*sustainability*

MDPI

*Article*

# Response Prediction of Asphalt Pavement in Cold Region with Thermo-Hydro-Mechanical Coupling Simulation

**Junling Si [1], Tatsuya Ishikawa [2,*], Daoju Ren [1], Kimio Maruyama [3] and Chigusa Ueno [3]**

[1] Graduate School of Engineering, Hokkaido University, Kita 13, Nishi 8, Kita-ku, Sapporo 060-8628, Japan; junling.si.h3@elms.hokudai.ac.jp (J.S.); daoju.ren.d5@elms.hokudai.ac.jp (D.R.)
[2] Faculty of Engineering, Hokkaido University, Kita 13, Nishi 8, Kita-ku, Sapporo 060-8628, Japan
[3] Civil Engineering Research Institute for Cold Region, Sapporo 062-8602, Japan; k.maruyama@ceri.go.jp (K.M.); ueno-c22aa@ceri.go.jp (C.U.)
* Correspondence: t-ishika@eng.hokudai.ac.jp

**Abstract:** Although the theoretical pavement structure design method (TPSDM) is widely used for designing asphalt pavements in Japan, it still exhibits certain limitations, such as not considering the variation in moduli of the base and subgrade layers due to water contents, freeze–thaw action, and stress states. This study aims to enhance Japanese TPSDM's accuracy by considering variations in the resilient modulus of environmental impacts, pavement materials, pavement structure, and traffic load actions to accurately calculate the mechanical responses and predict pavement fatigue life. Firstly, the study develops a 3D Thermo-Hydro-Mechanical (THM) model using the finite element method (FEM) to investigate temperature and moisture distributions of the pavement with time. Then, based on the numerical results of the moisture, temperature, and stress state obtained from the THM analysis, the constant resilient modulus of the base and subgrade layers in the Japanese TPSDM is replaced with a resilient modulus that considers the stress state and the combined effects of water content fluctuations and freeze–thaw action. Finally, the fatigue life of the pavement is calculated based on the obtained mechanical response in THM analysis. The reliability and validity of the proposed fatigue life prediction method are well verified by comparing the calculated with the actual pavement fatigue life. Results indicate that the modifications improve the Japanese TPSDM by considering the environmental impacts, traffic load actions, pavement materials, and pavement structure, thereby improving the accuracy of predicting the fatigue life of asphalt pavements, particularly in cold regions.

**Keywords:** THM coupled model; resilient modulus; freeze–thaw; fatigue life prediction



**Citation:** Si, J.; Ishikawa, T.; Ren, D.; Maruyama, K.; Ueno, C. Response Prediction of Asphalt Pavement in Cold Region with Thermo-Hydro-Mechanical Coupling Simulation. *Sustainability* **2023**, *15*, 13614. https://doi.org/10.3390/su151813614

Academic Editor: Ramadhansyah Putra Jaya

Received: 3 August 2023
Revised: 1 September 2023
Accepted: 1 September 2023
Published: 12 September 2023



## 1. Introduction

Asphalt pavement is a commonly used form of infrastructure exposed to various environmental impacts and traffic load actions. Recently, there has been increasing concern about the deepening of asphalt pavement damage. During the initial stage of service, most of the damage is usually on the pavement surface. However, damage can occur in the base and subgrade layers where the pavement has aged severely [1]. Therefore, accurately predicting the fatigue life of asphalt pavement requires a comprehensive understanding of its mechanical response to significant environmental impacts. This becomes especially crucial in cold regions where temperature variations, moisture fluctuations, and freeze–thaw action can significantly impact the performance and durability of asphalt pavements [2]. The Mechanistic-Empirical Pavement Design Guide (MEPDG) [3] in the United States uses various models to simulate the pavement structure and its response to traffic load actions, environmental impacts, and other factors that affect pavement performance. The MEPDG considers factors such as pavement material properties, layer thicknesses, and other design inputs to predict pavement distresses such as fatigue cracking and rutting [3]. The theoretical pavement structure design method (TPSDM), currently used in Japan, relies

on mechanical-empirical standards to simply and quickly estimate the failure loading number against rutting and fatigue cracking [4]. Nonetheless, it is essential to address the limitations of the TPSDM compared to the MEPDG, particularly concerning pavement material properties, environmental impacts, and design life aspects. Here, pavement material properties involve mechanical characteristics, like resilient modulus, while environmental impacts involve the influencing temperature variations, moisture fluctuations, and freeze–thaw action on pavement performance. The design life involves considering the impact of traffic loads on predicted fatigue life against cracking and rutting.

For the pavement material properties, the TPSDM assumes that the base course and subgrade layers are linear elastic materials with constant moduli under equivalent 49-kN wheel load conditions throughout the year. However, these geomaterials exhibit nonlinear elastic properties with strain levels exceeding $10^{-6}$, which can be estimated by resilient modulus ($M_r$) [5,6]. Thus, in the pavement response analysis of the MEPDG, the relationship between the stress state and resilient modulus is captured by using the universal constitutive equation (Equation (1)), which establishes a connection between the resilient modulus and various stress parameters, including bulk stress, octahedral shear stress, and atmospheric pressure at a specific location within the pavement [3].

$$M_{\mathrm{r}} = k_1 \cdot p_a \cdot \left(\frac{\theta}{p_a}\right)^{k_2} \cdot \left(\frac{\tau_{oct}}{p_a} + 1\right)^{k_3} \quad (1)$$

where $k_1$, $k_2$, and $k_3$ are regression constants; $p_a$ is atmospheric pressure; $\theta$ is bulk stress; and $\tau_{oct}$ is octahedral shear stress.

In addition, the performance of flexible pavements is significantly affected by environmental conditions [7–10]. External factors, such as precipitation, temperature, freeze–thaw cycles, and groundwater level, play a crucial role in determining the extent to which the environment can impact pavement performance. Internal factors, including the susceptibility of geomaterials to moisture and freeze–thaw damage and the infiltration potential of the pavement, also play a role in determining how the pavement will react to external environmental conditions [11–13]. In the numerical simulation, the resilient modulus of any element (including the base course layer and subgrade layer) is affected by the water content and the physical state of the geomaterial (e.g., frozen state, recovering state, and unfrozen state). According to the definitions of the MEPDG, the recovery period refers to the thawed geomaterial that is gradually returning to its state before freezing occurs. Hence, during this period, the resilient modulus is influenced by the number of days that have elapsed since thawing started [3]. Considering these aspects, it is essential to reproduce the external environmental impacts and explore their influences on the pavement materials during the pavement design process. The MEPDG suggests an Enhanced Integrated Climatic Model (EICM), which captures the change in water content and freeze–thaw action [14]. Additionally, Ishikawa et al. [11] examined the impact of freeze–thaw action and the concurrent seasonal fluctuations in water content, named as climate effect, on the resilient deformation characteristics of base course materials, while Lin et al. [15] examined the climate effect on the resilient modulus of subgrade soil to evaluate the mechanical behavior of asphalt pavement in cold regions.

Rutting is a common form of pavement distress, particularly under the condition of repeated traffic loads over time. To improve the reliability of predicting fatigue life, it is essential to consider not only the direct effects of factors such as traffic repetition on rutting but also the rate-hardening behavior of the pavement layers and the contribution of non-subgrade layers to rutting [14,16]. Additionally, the effect of principal stress axis rotation (PASR) is widely believed to significantly impact the mechanical performance of pavement materials [17–20]. Lin et al. [16] introduced an adjustment parameter based on the MEPDG rutting depth prediction model (Equation (2)) to modify the Japanese rutting

failure criterion and proposed the ratio of axial strain, estimated with axial stress and shear stress, as a quantitative measure to describe the increase in axial strain caused by PSAR.

$$\varepsilon_p(N) = \beta_1 k_1 \left(\frac{\varepsilon_0}{\varepsilon_r}\right) e^{-\left(\frac{\rho}{N}\right)^{\beta}} \varepsilon_v \quad (2)$$

where $\varepsilon_p(N)$ is the permanent strain for the layer/sub-layer; $N$ is the number of traffic repetitions; $\varepsilon_0$, $\beta$, and $\rho$ are material properties; $\varepsilon_r$ is the resilient strain imposed in laboratory testing to obtain material properties $\varepsilon_0$, $\beta$, and $\rho$; $\varepsilon_v$ is the average vertical resilient strain in the layer, which is calculated by a multi-layer elastic pavement response model; $\beta_1$ is the calibration factor for the unbound granular and subgrade materials; and $k_1$ is the global calibration coefficient.

This study aims to improve the TPSDM by incorporating various factors and elements to account for environmental impacts, traffic load actions, pavement materials, and pavement structure changes. Firstly, to study the temperature and moisture distributions of the pavement with time a three-dimensional (3D) Thermo-Hydro-Mechanical (THM) coupled model is developed by using the Finite Element Method (FEM). Subsequently, based on the moisture, temperature, and stress state obtained from THM analysis the constant elastic modulus of the base and subgrade layer in the TPSDM is replaced with the resilient modulus that considers the stress state and the combined effects of water content fluctuations and freeze–thaw action. Finally, the mechanical response of the pavement is obtained and the fatigue life of the pavement is calculated. This proposed analytical procedure is named the Mechanistic-Empirical Pavement Structure Coupled Analysis (MEPSCA). This study proposes the seamless integration of these advancements when considering the environmental impacts, such as thaw-weakening and moisture fluctuations, into the pavement performance evaluation in terms of transportation geotechnics. Additionally, this study tackles the issue of significant differences between actual performance life and design life, ultimately providing a more comprehensive pavement design method.

## 2. Overview of Proposed Design Method

The proposed design method represents a significant change in how pavement design is performed compared to the TPSDM. As shown in Figure 1, site conditions (traffic, environmental impacts, pavement materials properties, and structure) and construction conditions are first considered when proposing a new pavement trial design. The trial design is then evaluated for adequacy by predicting the fatigue life against key distresses.

Firstly, this study presents a 3D coupled model of THM processes using COMSOL Multiphysics [21], as shown in Figure 2. Based on a nonlinear elastic model and convergence analysis, the mechanical field is developed within the proposed coupled model. The thermal and hydraulic fields are established by the PDEs (partial differential equations). Secondly, this study uses ODEs (ordinary differential equations) to characterize the physical state of geomaterials and quantify the number of days passed during the recovery period on the element scale. Furthermore, modeling the geomaterials with a stress-dependent modulus is a typical coupling problem that involves a circular dependence among resilient modulus, matric suction, temperature, stress, and deformation. This circular dependence can be solved in the WF-PDEs (weak form partial differential equations) to define the stress-dependent modulus. Lastly, in a multi-layer elastic model, the structural response results (including stress and strain) can be generated by utilizing the resilient modulus, which is influenced by the stress state and environmental impacts. Based on empirical models, the structural response results (including stress and strain) can then estimate the expected allowable loading number against rutting and fatigue cracking. The method of modifying the rutting failure criterion by incorporating the MEPDG model and the PASR effect enhances the practicality of the rutting model. To validate the proposed method, this study conducts a comparative analysis to compare its predictions with those obtained using established pavement design methods. Additionally, field validation is conducted to

confirm the effectiveness of the method in real-world scenarios by monitoring pavement moisture content and temperature changes, as well as actual fatigue life and modulus.

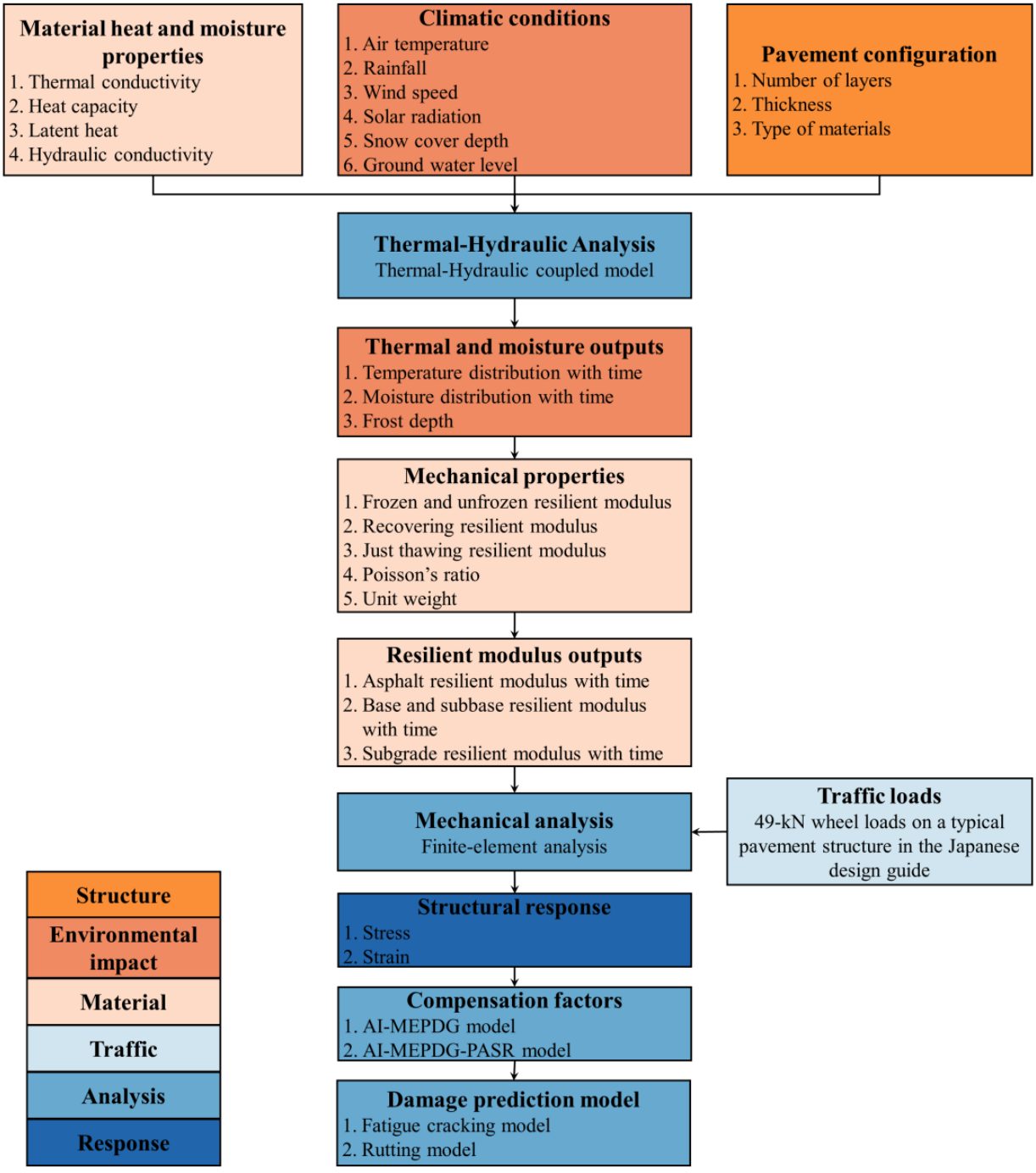


**Figure 1.** Scheme of the proposed MEPSCA.

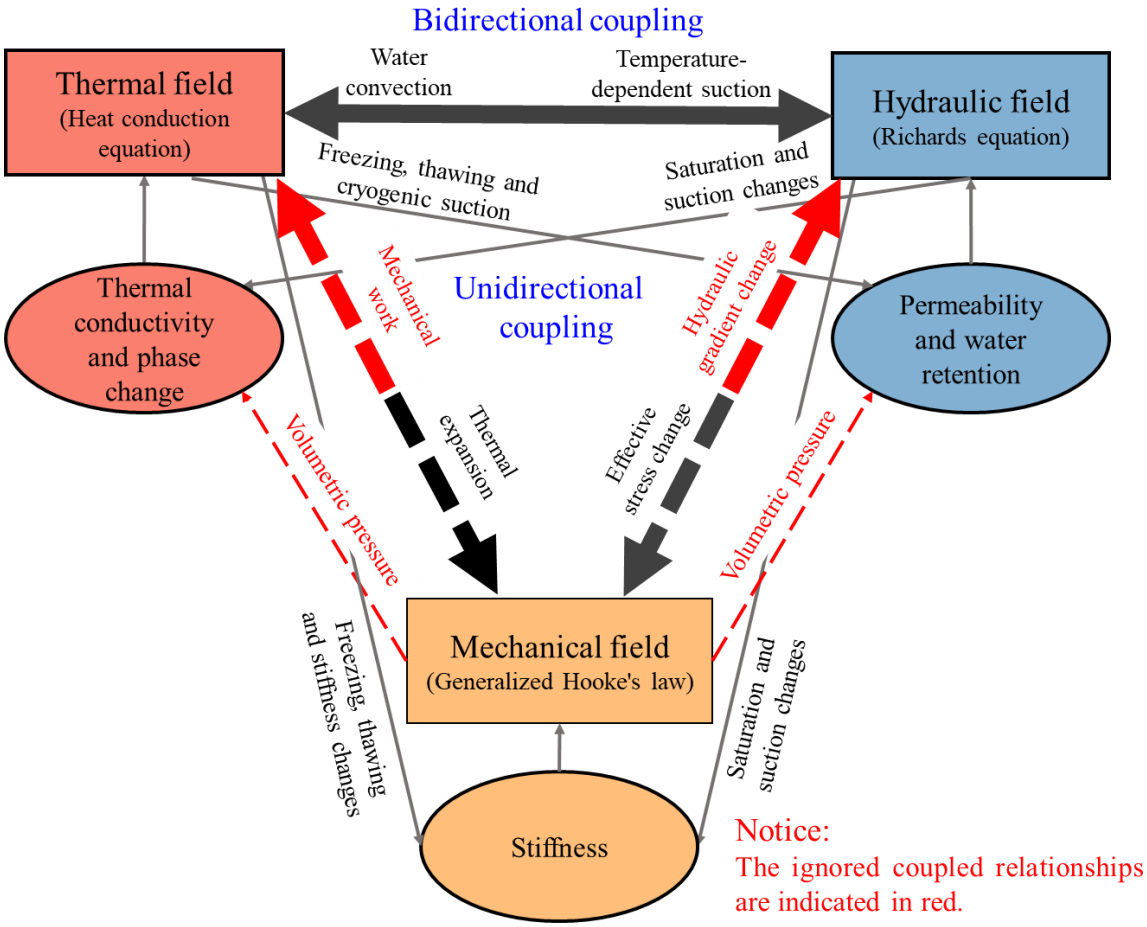


**Figure 2.** Scheme of THM coupled model.

## 3. Numerical Simulations for Evaluating the Environmental Impacts

### *3.1. Numerical Simulation Assumptions*

To establish the THM model, several fundamental assumptions are made, as follows:

1. The soil skeleton structure remains unchanged during freezing and thawing without considering frost heave and osmotic pressure for pure water.
2. The depression of the freezing point is assumed to be small.
3. The thermal expansion characteristics of pavement materials are not considered.
4. The pavement materials perform elastic behavior. Each layer is composed of homogeneous and isotropic material.
5. The layers are perfectly bound at their interfaces, and the conditions for continuity at the interfaces are satisfied.
6. The influence of volumetric pressure on the hydraulic and thermal fields is not considered.

### *3.2. Governing Equations and Basic Physical Parameters*

Since soils of the base course and subgrade layers of pavement structures are commonly in unsaturated conditions, the unsaturated–saturated seepage flow should be appropriately considered in the hydraulic field. The mass conservation equation can be formulated as Equation (3) [22].

$$C_H \frac{\partial u_w}{\partial t} + \frac{\rho_i}{\rho_w} n \frac{\partial S_i}{\partial t} = \nabla(k_w \nabla h) + f_w \quad (3)$$

where $C_H$ is the specific moisture capacity of soil; $u_w$ is the pore-water pressure; $k_w$ is the coefficient of water permeability; $h$ is the total hydraulic potential head which is the sum of the pore-water pressure head and elevation head; $n$ is porosity; $\rho_w$ and $\rho_i$ are the density of water and ice, respectively; $S_i$ is the degree of saturation for ice; $t$ is time; and $f_w$ is the sink/source term of mass.

The energy conservation equation used in the thermal analysis is as Equation (4) [23]:

$$C_{Ta}\frac{\partial T}{\partial t} + L\rho_i n\frac{\partial S_i}{\partial t} + \nabla \cdot (\lambda_T \nabla T) + C_{Tw}\nabla \cdot (\boldsymbol{v}_w T) = f_e \tag{4}$$

where $C_{Ta}$ is the apparent heat capacity of soil; $L$ is the latent heat of fusion of water; $\lambda_T$ is the thermal conductivity of soil; and $C_{Tw}$ is the volumetric heat capacity of water and $\boldsymbol{v}_w$ is the flux vector of water; $f_e$ is the sink/source term of energy; and $T$ is temperature.

Generalized Hooke's law can describe the stress–strain relationship of elastic materials, as shown in Equations (5) and (6) [24].

$$\{\sigma\} = [D](\{\varepsilon\} - \{\varepsilon_0\}) + \{\sigma_0\} \tag{5}$$

$$[D] = \frac{E}{(1+\mu)(1-2\mu)}\begin{bmatrix} 1-\mu & \mu & \mu & 0 & 0 & 0 \\ \mu & 1-\mu & \mu & 0 & 0 & 0 \\ \mu & \mu & 1-\mu & 0 & 0 & 0 \\ 0 & 0 & 0 & \frac{1-2\mu}{2} & 0 & 0 \\ 0 & 0 & 0 & 0 & \frac{1-2\mu}{2} & 0 \\ 0 & 0 & 0 & 0 & 0 & \frac{1-2\mu}{2} \end{bmatrix} \tag{6}$$

where $\{\sigma\}$ is the stress tensor; $\{\varepsilon\}$ is the elastic strain tensor; $\{\sigma_0\}$ is the initial stress; $\{\varepsilon_0\}$ is the initial strain; $[D]$ is the stiffness matrix; $E$ is the elastic modulus; and $\mu$ is Poisson's ratio.

Regarding the relative permeability of water, the van Genuchten (VG) model is adopted, as shown in Equations (7)–(9) [25].

$$k_w = k_{wr}k_s \tag{7}$$

$$k_{wr} = (S_e)^{1/2}\left[1 - \left(1 - S_e^{\frac{1}{m}}\right)^m\right]^2 \tag{8}$$

$$S_e = \frac{S_r - S_{rr}}{S_{rs} - S_{rr}} = \left[1 + (\alpha\psi)^\lambda\right]^{-m} \tag{9}$$

where $k_s$ is the permeability of saturated soil; $k_{wr}$ is relative hydraulic conductivity; $S_e$ is the effective degree of saturation; $S_r$ is the degree of saturation; $S_{rr}$ is the residual degree of saturation; $S_{rs}$ is the saturated degree of saturation; $\alpha$, $m$, $\lambda$ are VG model fitting parameters; $m = 1 - 1/\lambda$; and $\psi$ is matric suction.

The method for calculating the effective heat conductivity of the solid–fluid system as the weighted geometric mean of the conductivities of the fluid and the porous matrix is shown in Equation (10) [26].

$$\lambda_T = (\lambda_s)^{1-n}(\lambda_i)^{n-\theta_w}(\lambda_w)^{\theta_w} \tag{10}$$

where $\lambda_s$ is the heat conductivity of soil particles; $\lambda_i$ is the heat conductivity of ice; $\lambda_w$ is the heat conductivity of water; and $\theta_w$ is volumetric water content.

Similarly, the heat capacity of soil is the sum of the volumetric heat capacity of each component weighted by the respective volume, as shown in Equation (11) [27].

$$C_{Ta} = (1-n)C_{Tp} + nS_wC_{Tw} + nS_iC_{Ti} \tag{11}$$

where $C_{Tp}$ is the volumetric heat capacity of soil particles and $C_{Ti}$ is the volumetric heat capacity of ice.

The pressure head decrease obtained during the freezing process can be written as Equation (12) [28]:

$$\psi = \psi(T) = u_{w0} + \frac{L\rho_w}{T_0}(T - T_0) \tag{12}$$

Then, the Soil Water Characteristic Curve (SWCC) of VG model can be combined with the Clapeyron equation to estimate the effective degree of saturation for liquid water in unsaturated soil subjected to freeze–thaw action, as shown in Equation (13) [28].

$$S_e = \left[1 + \left(\alpha(u_{w0} + \frac{L\rho_w}{T_0}(T - T_0))\right)^{\lambda}\right]^{-m} \tag{13}$$

where $T_0$ is nominal freezing temperature and $u_{w0}$ is pore-water pressure (suction) before freezing.

### 3.3. Analytical Procedures

To evaluate the variation of resilient modulus of asphalt pavement depending on the weather conditions in cold regions, a 3D coupled THM FE analysis is conducted following the analytical flow chart shown in Figure 3.

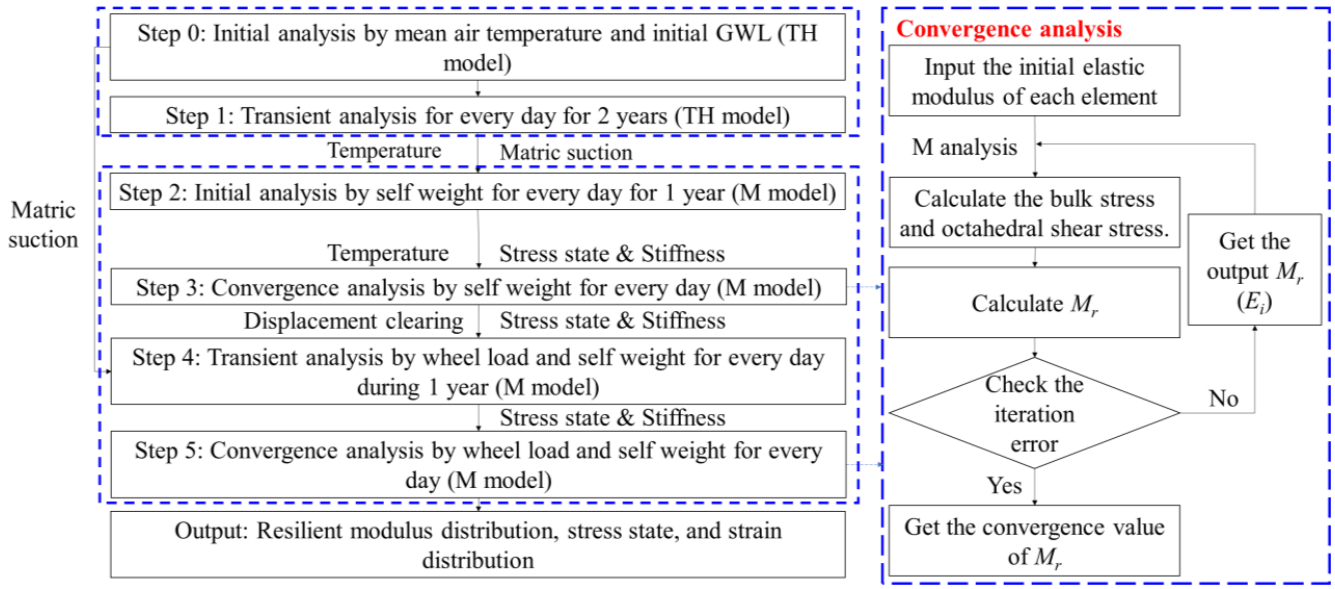


**Figure 3.** Flow chart of THM analysis and convergence analysis.

Among them, modeling the base course layer and subgrade soil with a stress-dependent modulus involves a circular interdependence between the resilient modulus, stress states, and deformation. Therefore, the convergence analysis of $M_r$ is necessary to determine the reliable layer-resilient modulus under a 49-kN wheel load [16]. This convergence analysis can be achieved by creating two additional Dependent Variables (DVs) in the WF-PDE to define the stress-dependent modulus. These two DVs will be defined in weak expressions and solved simultaneously with the other three defined DVs (i.e., displacement components) [29].

### 3.4. Numerical Model and Boundary Conditions

The Tomakomai test pavement FE model consists of the asphalt mixture layer (As layer), base course layer (C-40), anti-frost layer (C-80), and subgrade layer. Figure 4 shows the size, boundary conditions, and finite element mesh.

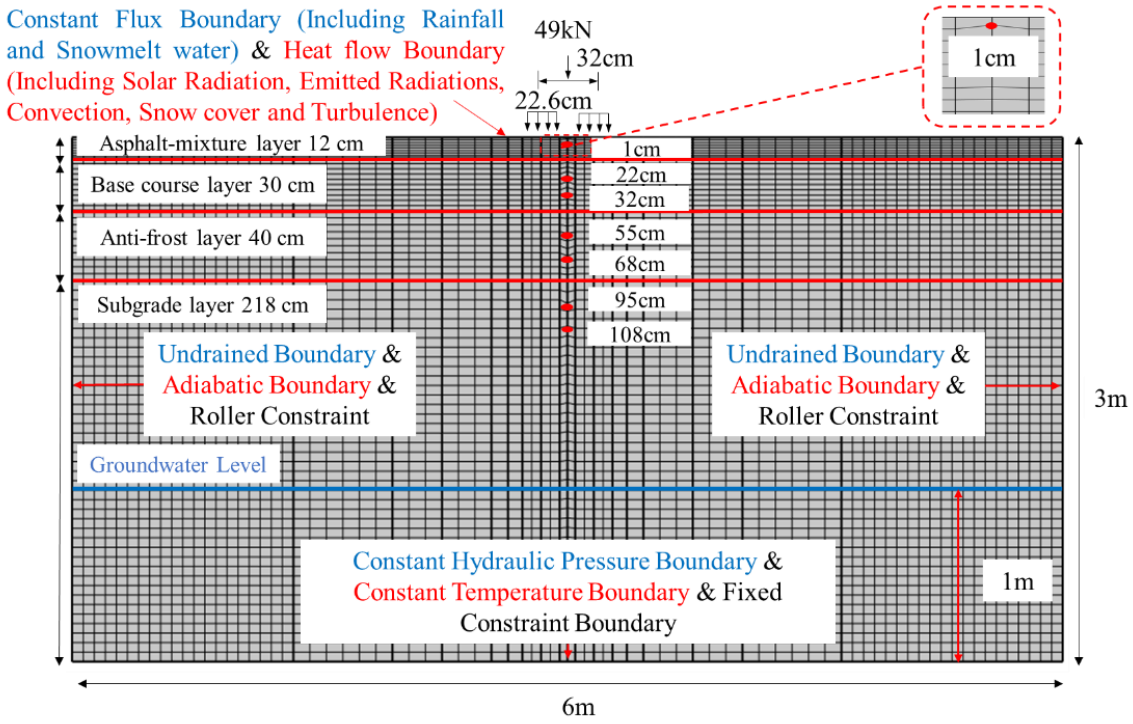


**Figure 4.** Boundary condition and finite element mesh.

In addition, to study the pavement performance and fatigue life the Civil Engineering Research Institute for Cold Region (CERI) designed and constructed eight test pavements in Bibi, Hokkaido [30]. Figure 5 illustrates the structures and length of each test pavement.

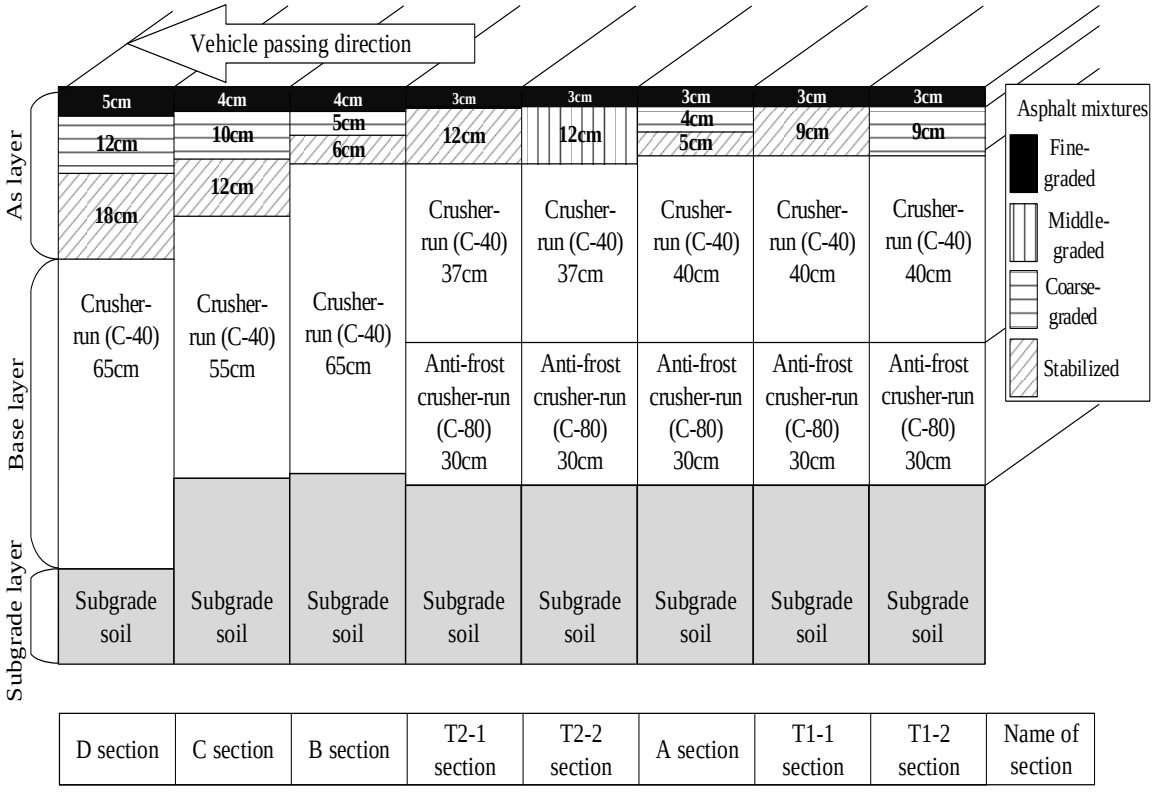


**Figure 5.** The pavement structure of Bibi test pavement.

### 3.5. Estimation of Precipitation

The precipitation, as the main reason driving changes in the hydraulic field, is estimated through Equations (14) and (15) [31].

$$P_{in} = (P_{rain} + SMWE) \tag{14}$$

$$SMWE = \frac{\rho_{snow}}{\rho_w} \Delta d \tag{15}$$

where $P_{rain}$ is rainfall; $SMWE$ is snow-melt water equivalent; $\rho_{snow}$ is snow density; and $\Delta d$ is the value of decreasing snow depth per day.

As for the snow density, Zhu et al. [32] summarized different models for predicting the snow density and proposed the SY08 (Shinme et al.) [33]-E86 (Endo) [34] combination model for calculating snow density in Hokkaido, Japan.

### 3.6. Modeling Upper and Lower Surface Thermal Boundaries

The temperature of the pavement-soil system is determined by a complex balance that occurs at the interface between the pavement and the air. In this case, the main factors affecting the pavement thermal regime include solar radiation, emitted radiations, convection, and turbulence. This study incorporates these factors when setting the upper surface thermal boundary. It is noted that this study adopted various meteorological data from the Automated Meteorological Data Acquisition System (AMeDAS) [35].

The total solar radiation ($Q$) received at the surface, shown in Equation (16), is the sum of direct and diffuse radiation [36].

$$q_s = \alpha_s Q \tag{16}$$

where $q_s$ is the net short-wave radiation received and $\alpha_s$ is the absorptivity of the pavement surface to solar radiation, taken as 0.9 in the case of the asphalt mixture or 0.5 in the case of snow cover [36].

A perfect radiator emits radiation ($q_{er}$), and the intensity is proportional to the fourth power of its temperature ($T$) as predicted by the Stefan–Boltzmann equation (Equation (17)) [37]:

$$q_{er} = \varsigma \epsilon_s \left( T_s^4 - T_a^4 \right) \tag{17}$$

where $\varsigma$ is the Stefan–Boltzmann constant ($5.67 \times 10^{-8}$ W/m$^2$ K$^4$); $\epsilon_s$ is surface emissivity, taken as 0.9 in case of the asphalt mixture [37]; and $T_s$ and $T_a$ are the temperatures of the surface and the atmosphere, respectively.

Heat extraction by convection ($q_c$) is a function of the temperature difference between the ground surface and the atmosphere, as expressed in Equation (18) [37].

$$q_c = h_c (T_s - T_a) \tag{18}$$

where $h_c$ is the convective heat transfer coefficient.

Zarling and Braley [38] have proposed the following dimensional relationship (Equation (19)) to determine the convective heat transfer coefficient for a smooth surface as a function of wind speed:

$$h_c = 5.678 + 1.056U \tag{19}$$

where $U$ is wind speed.

The energy flux through the snow ($q_{sn}$) when there is snow cover on the ground is estimated using Equation (20) [39].

$$q_{sn} = -\lambda_{sn} \frac{(T_s - T_a)}{d_{sn}} \tag{20}$$

where $\lambda_{sn}$ is the thermal conductivity of snow cover, taken as 0.255 W/m·°C [40] and $d_{sn}$ is snow depth.

On the other hand, this study assumes that the heat flow from inside the earth is negligible. Then, the temperature ($T_z$) at the depth of the lower surface thermal boundary ($z$) can be calculated as Equation (21) [36]:

$$T_z = T_m + A \cdot \exp\left(-z\sqrt{\frac{\pi}{\alpha_u p_d}}\right) \cdot \sin\left(\frac{2\pi t}{p_d} + \varphi - z\sqrt{\frac{\pi}{\alpha_u p_d}}\right) \quad (21)$$

where $T_m$ is the mean annual ground surface temperature; $A$ is the ground surface temperature amplitude; $\varphi$ is the initial phase; $p_d$ is the period (365 days); $z$ is the depth of the lower surface thermal boundary, set as 3 m in this study; and $\alpha_u$ is the thermal diffusivity, $5.17 \times 10^{-2}$ m$^2$/day [36].

### 3.7. Material Input Parameters

The material input parameters used in this study are listed in Table 1. For all layers, the soil parameters are determined reasonably simply and robustly from laboratory tests. The parameters in Equations (7)–(9) were obtained through parameter fitting and based on the water retention and permeability test data [41,42]. The thermal conductivity and volumetric heat capacity are based on the thermal properties test [43]. The dry density of soil, porosity, and Poisson's ratio are based on the field surveys. The value of constants $k_1$ to $k_4$ and $F_{clim}$ in Equation (23) are determined through regression analysis on resilient modulus test results of C-40 and Tomakomai soil [16].

**Table 1.** Material input parameters in THM analysis [16,35,41–43].

| Parameters | Unit | As Layer | Base Course Layer | Anti-Frost Layer | Subgrade Layer |
|---|---|---|---|---|---|
| Thermal conductivity ($\lambda_T$) | W/m·°C | 1.45 | 2.51 | 2.13 | 1.61 |
| Dry density of soil ($\rho_d$) | kg/m$^3$ | 2400 | 1800 | 1800 | 1200 |
| Saturated degree of saturation ($S_{rs}$) | % | 100 | 100 | 100 | 100 |
| Residual degree of saturation ($S_{rr}$) | % | 20 | 32.30 | 32.30 | 25.41 |
| Poisson's ratio ($\mu$) | - | 0.35 | 0.35 | 0.35 | 0.4 |
| van Genuchten fitting parameter ($\alpha$) | 1/kPa | 2.33 | 12.17 | 12.17 | 0.985 |
| van Genuchten fitting parameter ($\lambda$) | - | 1.94 | 1.56 | 1.56 | 1.71 |
| Permeability of saturated soil ($k_s$) | m/s | $1.5 \times 10^{-4}$ | $1.0 \times 10^{-3}$ | $1.0 \times 10^{-3}$ | $1.72 \times 10^{-7}$ |
| Volumetric heat capacity of soil particles ($C_{Tp}$) | J/m$^3$·°C | $1.8 \times 10^6$ | $1.8 \times 10^6$ | $1.8 \times 10^6$ | $0.86 \times 10^6$ |
| Porosity ($n$) | - | 0.07 | 0.24 | 0.24 | 0.55 |
| Regression constants ($k_1$) | - | - | 3.042 | 3.042 | 0.526 |
| Regression constants ($k_2$) | - | - | 0.886 | 0.886 | 1.293 |
| Regression constants ($k_3$) | - | - | −1.696 | −1.696 | −2.650 |
| Regression constants ($k_4$) | - | - | 1.076 | 1.076 | 1.008 |
| Regression constants ($F_{clim}$) | - | - | 0.749 | 0.749 | 0.948 |

### 3.8. Verification of the Thermo-Hydro Field of Model

Figure 6 compares ground temperature changes at different depths obtained through FE simulation and measurement data. From Figure 6, it is revealed that the fluctuation in ground temperature becomes remarkable at the shallow part of pavement structure. This indicates that the closer to the ground, the more significant the environmental impacts on the ground temperature. From comparing the ground temperature and freezing duration between simulation results and measurement data, it is recognized that the annual change in the ground temperatures obtained from the proposed FE simulation is almost consistent with the measured results, irrespective of the ground depth.

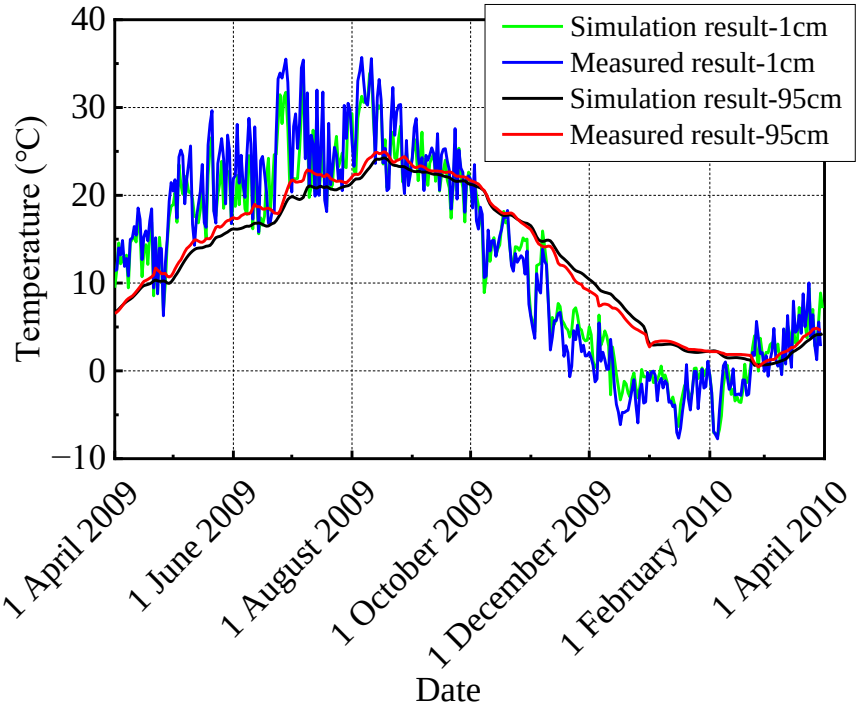


**Figure 6.** Ground temperature at different depths.

Figure 7 compares the variation of frost-penetration depth with time between the measurement data and the simulation results. Here, the frost-penetration depths of both measurements and simulations were estimated by the linear interpolation of ground temperatures at the adjacent depths at a position of 0 °C isotherm. The frost-penetration depth reached the anti-frost layer in 2009 and decreased dramatically as the temperature rose, starting in March. It is seen that the FE simulation poorly reproduces the measured frost-penetration depth as compared to the ground temperature. A reason for this is that when the ground temperature becomes close to 0 °C the linear interpolation is not precise. Meanwhile, Figure 8 shows the changes in the frost penetration depth under three other conditions: dry conditions, saturated conditions, and static water content distribution (water content distribution controlled by groundwater level). It can be seen from Figure 8 that there is little change in the frost penetration depth between the static water content distribution and the dynamic water content distribution. However, in dry conditions, the change in frost penetration depth is more significant due to the smaller heat capacity and no latent heat effect. If water content distribution is not considered, the frost penetration depth will be overestimated during the cooling process and underestimated during the warming process. The comparison results in the thermal field indicate that the proposed FE simulation is reliable for estimating the thermal field of the asphalt pavement.

Furthermore, as shown in Figure 8, there is a noticeable trend of the degree of saturation of the base course layer rapidly decreasing after late December 2009. This is due to the freezing of pore water at a ground temperature lower than the freezing temperature. During the thawing season in March, the water accumulated by frost heave during winter and snowmelt water contribute to high moisture levels in the pavement structure. This change in water content, observed from the regular season to the thawing season, significantly affects the mechanical behavior of the base course and subgrade layers. The comparison results in Figure 8 in the hydraulic field demonstrate the high reliability of the proposed finite element simulation to evaluate the infiltration behavior of the asphalt pavement.

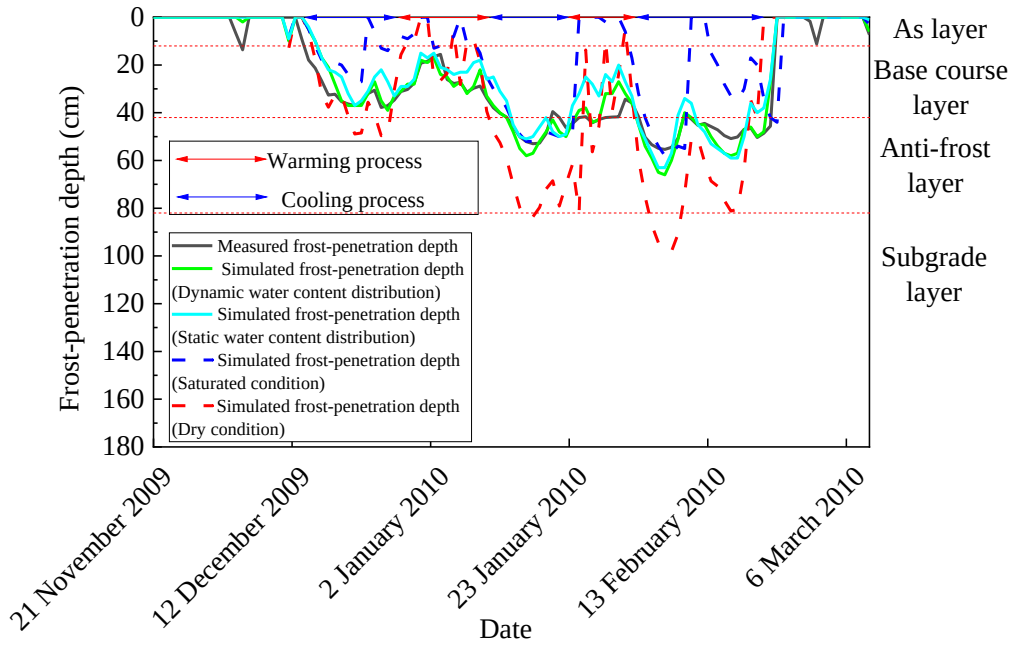


**Figure 7.** Frost-penetration depth curve over time.

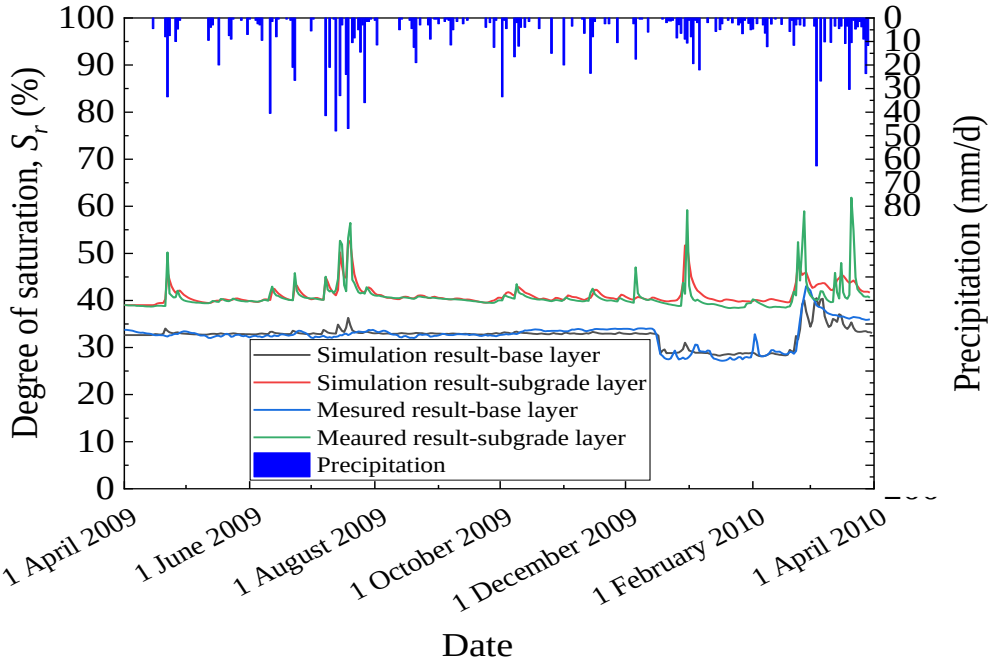


**Figure 8.** Degree of saturation curve over time.

## 4. Resilient Modulus Estimation of Pavement Considering the Environmental Impacts

It is widely acknowledged that environmental impacts such as temperature and moisture directly affect pavement material behavior and pavement performance. However, the effect of moisture on asphalt mixtures is insignificant compared to geomaterials. On the other hand, temperature affects both the asphalt and unbound layers significantly. Consequently, it is essential to assess the resilient pavement modulus in response to environmental impacts following the acquisition of temperature and water content data in the preceding section.

### *4.1. Evaluation of Temperature-Dependent Resilient Modulus of the Asphalt Layer*

Zhang et al. [44] proposed a reasonable method for predicting the elastic modulus of the As layer at different temperatures based on the elastic modulus of the asphalt mixture obtained from laboratory element tests, as shown in Equation (22).

$$E_1 = a \times \arctan(bT_1 + c) + d \quad (22)$$

where $E_1$ is the elastic modulus of the As layer; $a$, $b$, $c$, $d$ are regression constants; and $T_1$ is the average temperature of the As layer. When $T_1 < 10$ °C, the relationships between the elastic modulus of the As layer ($E_1$) obtained from FWD (Falling Weight Deflection) tests and the temperature of the As layer ($T_1$, daily average or during FWD test) are shown in Figure 9.

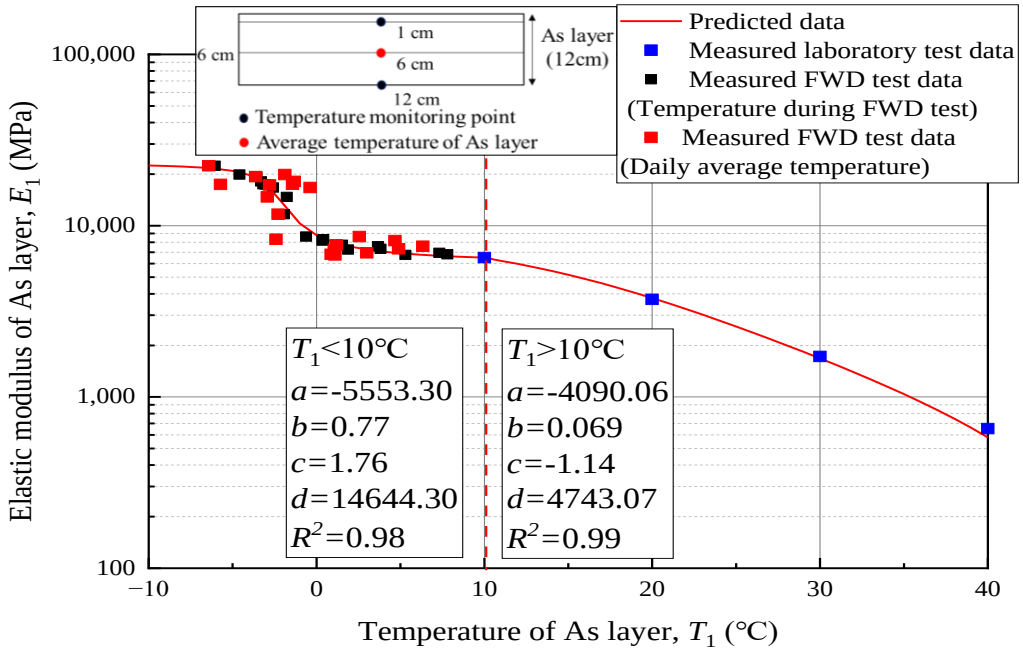


**Figure 9.** Relationship between the elastic modulus of the As layer and temperature.

To complement the measured data of $E_1$ at higher $T_1$, the $E_1$-$T_1$ relationships obtained from 4PBF (Four-Point Bending Fatigue) tests are added when $T_1 \geq 10$ °C. In addition, the regression analysis using Equation (22) is conducted on the $E_1$-$T_1$ relationships. The regression results are shown in Figure 9. Here, by averaging the temperatures measured at two monitoring points with different depths shown in Figure 9, the temperature of the As layer ($T_1$) was calculated at a depth of 6 cm under the ground surface. It is noted that the regression result was obtained by fitting the relationship between the elastic modulus of the As layer and the temperature during the FWD test or 4PBF test separately. It is recognized that Equation (22) can reflect the relationships between the elastic modulus of the As layer and the temperature during tests. Accordingly, through the daily average temperature of the As layer, the change in the daily average elastic modulus of the As layer with time can be estimated.

### *4.2. Effects of Soil Moisture Variations and Freeze–Thaw Action on Resilient Modulus*

Moisture and temperature are the two environmentally driven variables that can significantly impact the resilient modulus of geomaterials. However, moisture has two distinct effects: it can influence the state of stress through suction or pore water pressure, and it can affect the soil structure by destroying cementation between particles. In freezing temperatures, the water in the soil freezes, causing the resilient modulus to increase to values higher than before freezing. This process may also create ice lenses, resulting in

areas of significantly reduced strength in the pavement upon thawing. Only considering constant modulus will lead to inaccuracy and large variability [45]. Therefore, in this study, evaluating the resilient modulus of the base and subgrade layers affected by moisture fluctuations and freeze–thaw action is necessary.

Lin et al. [15] proposed a simple model to estimate the climate effect on the resilient modulus by considering the synergistic effects between water content and freeze–thaw action, as shown in Equation (23).

$$M_r = F_{clim} \cdot k_1 p_a \left(\frac{\sigma_{ii}}{p_a}\right)^{F_{clim} \cdot k_2} \left(\frac{\tau_{oct}}{p_a} + 1\right)^{F_{clim} \cdot k_3} \left(\frac{\psi}{\sigma_{net}} + 1\right)^{F_{clim} \cdot k_4} \quad (23)$$

where $F_{clim}$ is the climatic factor; $k_1$, $k_2$, $k_3$, $k_4$ are regression constants; $\sigma_{ii}$ is bulk stress (kPa), defined as $\sigma_1 + \sigma_2 + \sigma_3$; $\sigma_{net}$ is net mean stress (kPa), defined as $(\sigma_{ii}/3 - u_a)$; and $u_a$ is pore air pressure, set as 0 kPa in this study.

Meanwhile, the influence of loading frequency needs to be considered when using the results of laboratory element tests, as the loading frequency used in the FWD test is 50 Hz [46], while the loading frequencies in Ishikawa et al. [11] and Lin et al. [15] are 10 Hz and 0.2 Hz, respectively. Equations (24)–(26) were proposed to describe the loading rate effect on the resilient modulus [47].

$$\frac{E(f)}{E(0.5\text{ Hz})} = 1 + F(\psi) * log(f) \quad (24)$$

$$F(\psi) = 0.06153 - 0.02043 \times 0.68826^{\psi} \quad (25)$$

$$E(50\text{ Hz}) = \left(\frac{E(50\text{ Hz})}{E(0.5\text{ Hz})} / \frac{E(f)}{E(0.5\text{ Hz})}\right) E(f) = \left(\frac{1 + F(\psi) \times \log(50)}{1 + F(\psi) \times \log(f)}\right) E(f) \quad (26)$$

where $f$ is the loading frequency; $E\ (0.5\text{Hz})$ is the resilient modulus obtained at $f$ = 0.5 Hz; $E(f)$ is the predicted resilient modulus at any frequency $(f)$; and $F(\psi)$ is referred to as the frequency effect, which is affected by matric suction $(\psi)$ [15]. Through Equation (26), derived from Equations (24) and (25), the resilient modulus of base course layer, $E_2\ (10\text{ Hz})$ obtained from Ishikawa et al. [11] and the resilient modulus of subgrade soil, $E_3\ (0.2\text{ Hz})$ obtained from Lin et al. [15] were converted to the resilient modulus ($E_2(50\text{ Hz})$ and $E_3\ (50\text{ Hz})$) of FWD test.

To help visualize possible changes in resilient modulus caused by changes in the physical state with time, a time-depth diagram for a typical pavement structure is presented in Figure 10. Here, the frozen state (blue, denoted $M_{rF}$) is one where the soil temperature is lower than freezing temperature, while the recovering state (red, denoted $M_{rR}$) is one where the soil temperature is higher than freezing temperature after freezing. Another state is the unfrozen state (orange, denoted $M_{rU}$). Notably, the coexistence of these four physical states is possible within a given layer.

The following description outlines a methodology for estimating physical states, demonstrating the calculation of adjustment factors for each element in all three cases. For the behavior of base and subgrade layers, the absolute modulus of frozen geomaterials is obtained according to the on-site FWD test. Though the resilient modulus estimated by Equation (23) can evaluate the minimum resilient modulus during just thawing state, there is a possibility that with time passing the reduced resilient modulus recovers to an unfrozen state. Therefore, for recovering geomaterials, the resilient modulus exhibits a time-dependent increase that ranges from the just thawing state ($M_{rmin}$) to the unfrozen state ($M_{rU}$). This increase can be quantified by the recovery ratio ($RR$) on a scale from 0 to 1, as shown in Equation (27) [14]. Accordingly, the configuration method of climatic factors ($F_{clim}$) during the recovery period in numerical simulation can be obtained, as shown in Equation (28).

$$RR = \frac{T_{R,s}}{T_R} \quad (27)$$

$$F_{clim} = \left(F_{clim,min} + RR(1 - F_{clim,min})\right) \tag{28}$$

where $T_{R,s}$ is the number of days elapsed from thawing started in numerical simulation; $T_R$ is the number of days required for a given geomaterial from thawed state to unfrozen state [14]; and $F_{clim,min}$ is the minimum of climatic factor during just thawing state.

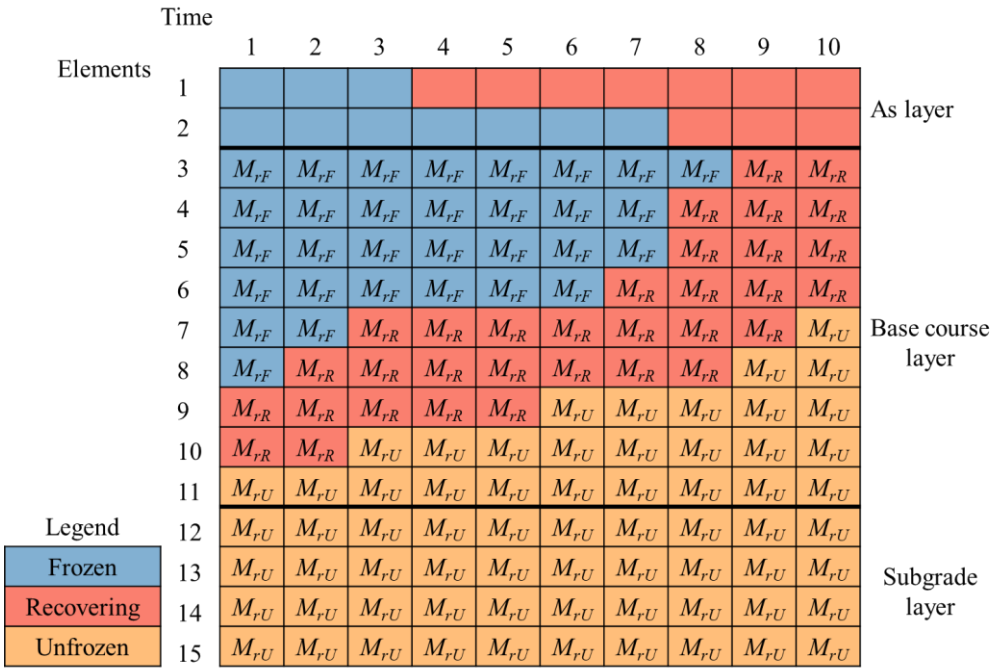


**Figure 10.** Time-depth diagram of a typical pavement structure.

However, when the temperature exceeds the freezing temperature, the physical state of a geomaterial cannot be determined solely based on temperature, as it may exist in an unfrozen or thawed state. Consequently, in this study, Equations (29)–(34) and five intermediate variables (*IV*s) were employed to ascertain the recovery state of soil elements and the number of days elapsed since thawing started ($T_{R,s}$). Figure 11 illustrates the correlation between temperature and various intermediate variables during simulation. Initially, the $IV_0$ is defined, followed by obtaining $IV_2$ through two integrations (Equations (29)–(31)). This latter variable is employed to describe the physical condition of each element, as shown in Equation (32). Notably, when $IV_2$ is greater than zero and the temperature is also above freezing temperature the element is in a recovering state. Conversely, when $IV_2$ is equal to zero and the temperature is above freezing temperature the element remains in an unfrozen state. Finally, when the temperature drops below freezing temperature the element transitions into a frozen state.

$$IV_0 = \begin{cases} 1, & T \le T_0 \\ 0, & T > T_0 \end{cases} \tag{29}$$

$$IV_1 = \int IV_0 dt \tag{30}$$

$$IV_2 = \begin{cases} 0, & T \le T_0 \\ IV_1, & T > T_0 \end{cases} \tag{31}$$

$$\begin{cases} T \le T_0\,, & \text{Frozenstate} \\ IV_2 > 0 \ \wedge \ T > T_0, & \text{Recovering state} \\ IV_2 = 0 \ \wedge \ T > T_0, & \text{Unfrozen state} \end{cases} \tag{32}$$

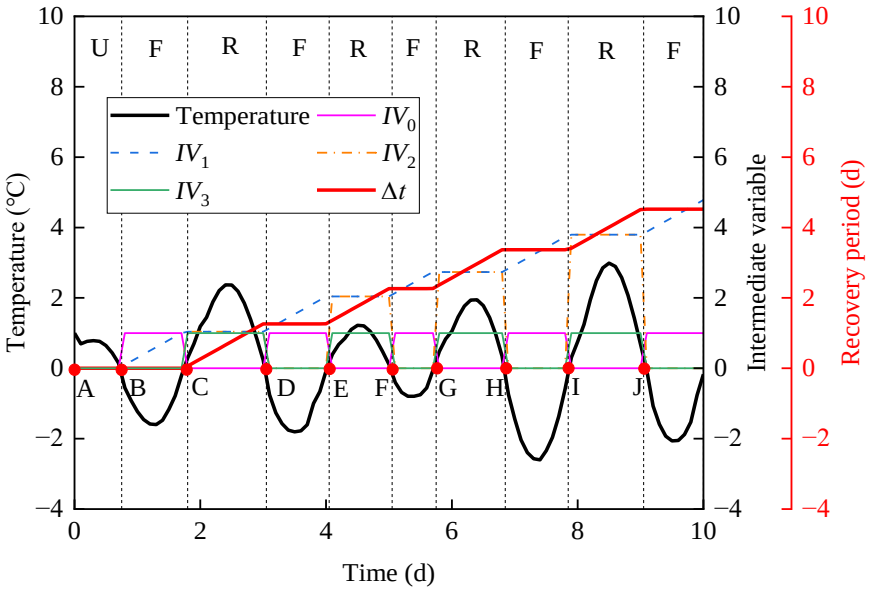


**Figure 11.** The relationship between element temperature and recovery period.

To precisely quantify the number of days elapsed in the recovery period (excluding the frozen period) of each element, the normalization of $IV_2$ to obtain $IV_3$ is undertaken (Equation (33)), followed by the integration of the latter to derive $T_{R,s}$, as shown in Equation (34).

$$IV_3 = \begin{cases} 0, & IV_2 \le 0 \\ 1, & IV_2 > 0 \end{cases} \tag{33}$$

$$T_{R,s} = \int IV_3 dt \tag{34}$$

In summary, the expressions for the resilient modulus of the base and subgrade layers as a function of climatic factors and loading frequency can be derived, as shown in Equations (35) and (36).

$$E_2(50\ \text{Hz}) = \begin{cases} M_{rF} = 1120\ \text{MPa} \\ M_{rU} = \frac{E(50\text{Hz})}{E(10\text{Hz})} k_1 p_a \left(\frac{\sigma_{ii}}{p_a}\right)^{k_2} \left(\frac{\tau_{oct}}{p_a} + 1\right)^{k_3} \left(\frac{\psi}{\sigma_{net}} + 1\right)^{k_4} \\ M_{rmin} = \frac{E(50\text{Hz})}{E(10\text{Hz})} F_{clim,\ min} \cdot k_1 p_a \left(\frac{\sigma_{ii}}{p_a}\right)^{F_{clim,\ min} \cdot k_2} \left(\frac{\tau_{oct}}{p_a} + 1\right)^{F_{clim,\ min} \cdot k_3} \left(\frac{\psi}{\sigma_{net}} + 1\right)^{F_{clim,\ min} \cdot k_4} \\ M_{rR} = \frac{E(50\text{Hz})}{E(10\text{Hz})} F_{clim} \cdot k_1 p_a \left(\frac{\sigma_{ii}}{p_a}\right)^{F_{clim} \cdot k_2} \left(\frac{\tau_{oct}}{p_a} + 1\right)^{F_{clim} \cdot k_3} \left(\frac{\psi}{\sigma_{net}} + 1\right)^{F_{clim} \cdot k_4} \end{cases} \tag{35}$$

$$E_3(50\ \text{Hz}) = \begin{cases} M_{rF} = 200\ \text{MPa} \\ M_{rU} = \frac{E(50\text{Hz})}{E(0.2\text{Hz})} k_1 p_a \left(\frac{\sigma_{ii}}{p_a}\right)^{k_2} \left(\frac{\tau_{oct}}{p_a} + 1\right)^{k_3} \left(\frac{\psi}{\sigma_{net}} + 1\right)^{k_4} \\ M_{rmin} = \frac{E(50\text{Hz})}{E(0.2\text{Hz})} F_{clim,\ min} \cdot k_1 p_a \left(\frac{\sigma_{ii}}{p_a}\right)^{F_{clim,\ min} \cdot k_2} \left(\frac{\tau_{oct}}{p_a} + 1\right)^{F_{clim,\ min} \cdot k_3} \left(\frac{\psi}{\sigma_{net}} + 1\right)^{F_{clim,\ min} \cdot k_4} \\ M_{rR} = \frac{E(50\text{Hz})}{E(0.2\text{Hz})} F_{clim} \cdot k_1 p_a \left(\frac{\sigma_{ii}}{p_a}\right)^{F_{clim} \cdot k_2} \left(\frac{\tau_{oct}}{p_a} + 1\right)^{F_{clim} \cdot k_3} \left(\frac{\psi}{\sigma_{net}} + 1\right)^{F_{clim} \cdot k_4} \end{cases} \tag{36}$$

### *4.3. Verification of the Mechanical Field of Model*

To analyze the impact of weather conditions on the resilient modulus, five specific weather conditions shown in Table 2 have been selected for separate evaluation. This analysis involves studying the distribution of the resilient modulus under each weather condition. Additionally, comparative analysis considers specific on-site testing dates for

different projects. Furthermore, the Bibi test pavement's service period from 1990 to 2004 resulted in most of the measured results being within this period.

**Table 2.** Selection of weather conditions.

| | **Regular Season -Sunny Day** | **Regular Season -Rainy Day** | **Freezing Season** | **Partial Thawing Season** | **Thawing Season** |
|---|---|---|---|---|---|
| | 10 May 2009 | 20 July 2009 | 7 February 2010 | 22 February 2010 | 4 March 2010 |
| Situation description | No rainfall | Rainfall reaches the maximum | Frost-penetration depth reaches the maximum | A typical Sandwich-Structure | Snowmelt water reaches the maximum |

The distributions of resilient modulus within the pavement in different seasons are plotted in Figure 12. It is evident that the As layer exhibits a varying resilient modulus distribution with depth, which is mainly attributed to temperature. In winter, the surface temperature is lower than the internal temperature, while in the regular and thawing seasons the surface temperature is higher than the internal temperature. From Figure 12, it can be found that the resilient modulus increases as the depth increases due to the bulk stress of soils increasing, and the octahedral shear stress is weakened along with the depth. Under the center of wheel loads, the resilient modulus at the surface of the base course layer changes significantly due to the stress concentration in this area. It can also be found that in the thawing season and rainy days, higher water content dramatically reduces the resilient modulus of the base course layer and subgrade layer, and freezing action improves the resilient modulus of the base course layer. Moreover, the resilient modulus above the groundwater level increases with increasing the matric suction away from the groundwater level. The resilient modulus below the groundwater level increases with increasing bulk stress as the matric suction keeps zero.

To verify the efficiency and effectiveness of the developed MEPSCA, an investigation was conducted to study the reduced bearing capacity of the base and subgrade layers during the thawing season in cold regions. Figure 13 displays the distribution of the degree of saturation and resilient modulus of the As layer, base layer, and anti-frost layer without a wheel load as of 22 February 2010, when thawing had progressed after freezing, as the previous analysis results determined. The depth in Figure 13 indicates the distance from the ground surface. While the As and base layers have thawed, the base layer has only thawed near the upper area, with the rest still frozen. The degree of saturation near the thawed base layer has increased, resulting in decreased resilient modulus near the upper area of the base layer. This is because when rainwater or snowmelt flows into the base layer, the frozen area has lower permeability than the thawed area, resulting in stagnant water at the upper boundary of the frozen area. These results partially reflect the importance of evaluating the environmental impacts on the fatigue life of pavement structures in cold regions.

The resilient modulus estimated through FE simulation is compared with the measured resilient modulus in Figure 14. Although the MEPSCA can provide the resilient modulus of each element, to make a reasonable comparison with the measured value it is necessary to use the average method to evaluate the overall resilient modulus of the pavement. The volume average resilient modulus within a range of 1.5 m on both sides of the load center is calculated in the FE simulation, which is consistent with the deflection recorded by the FWD test within a range of 1.5 m around the load center [11].

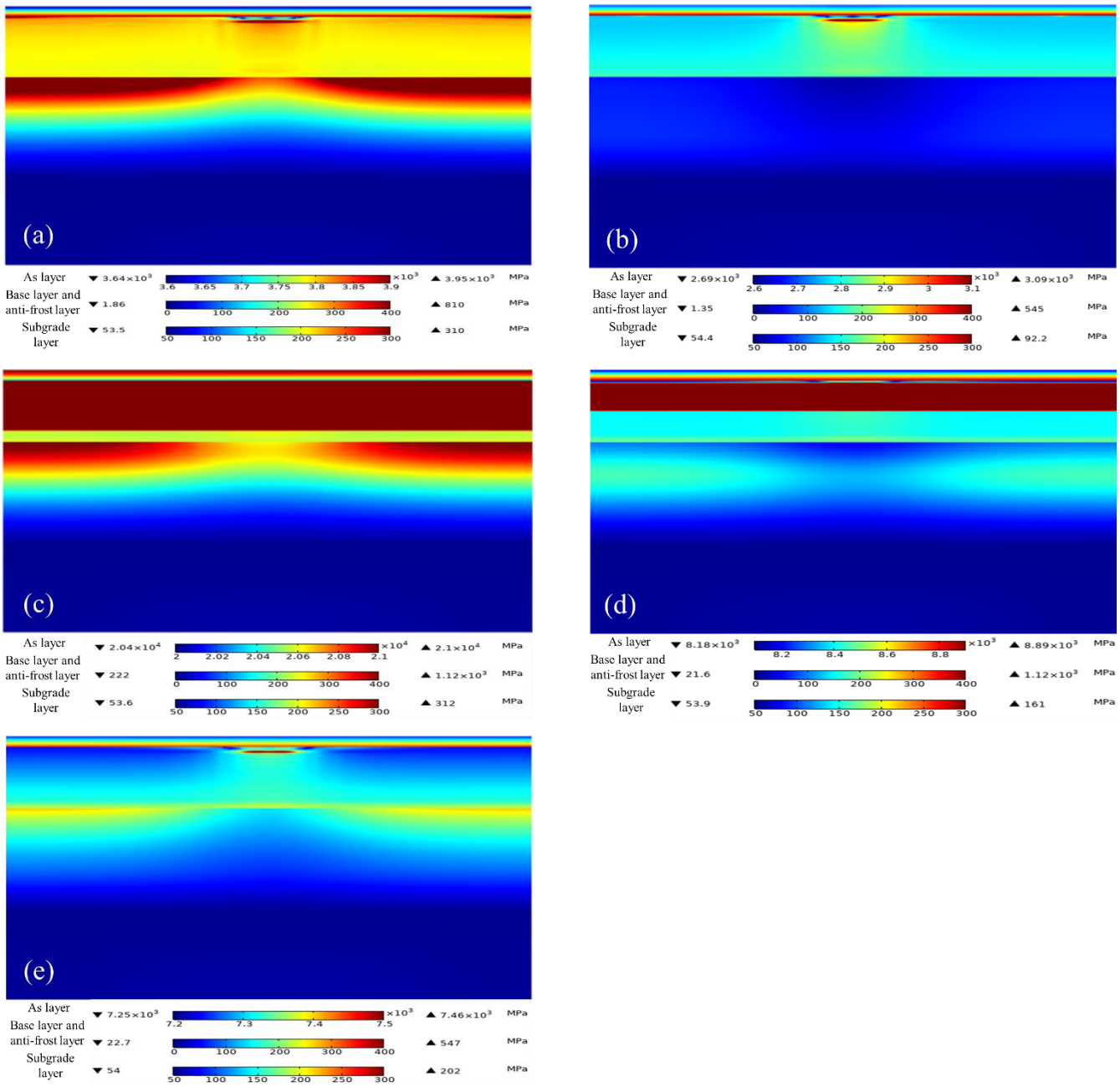


**Figure 12.** Resilient modulus distribution in different seasons ((**a**) regular season-sunny day; (**b**) regular season-rainy day; (**c**) freezing season; (**d**) partial thawing season; (**e**) thawing season).

Based on Figure 14, it can be seen that the resilient modulus of the base course layer is greatly affected by the frost-penetration depth during the freezing season. Due to the influence of weather conditions in the thawing season, the resilient modulus decreases dramatically, which may significantly impact the fatigue life of the pavement. On the other hand, the resilient modulus of the subgrade layer resilient modulus is notably influenced by changes in water content. Overall, the simulation method proposed in this study can effectively capture the variation of pavement resilient modulus over time.

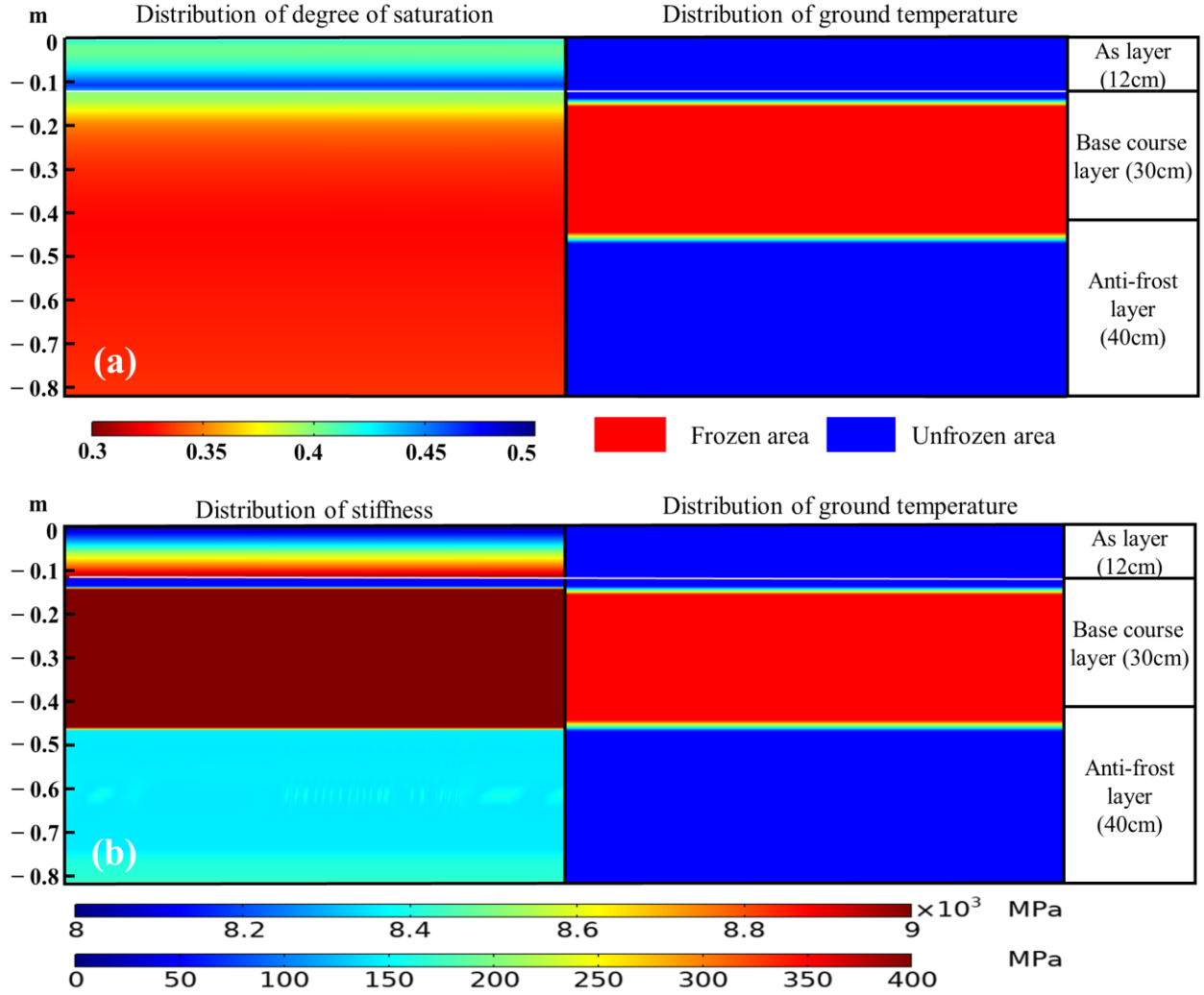


**Figure 13.** Distribution of the resilient modulus and degree of saturation during the freezing and thawing process ((**a**) resilient modulus; (**b**) degree of saturation).

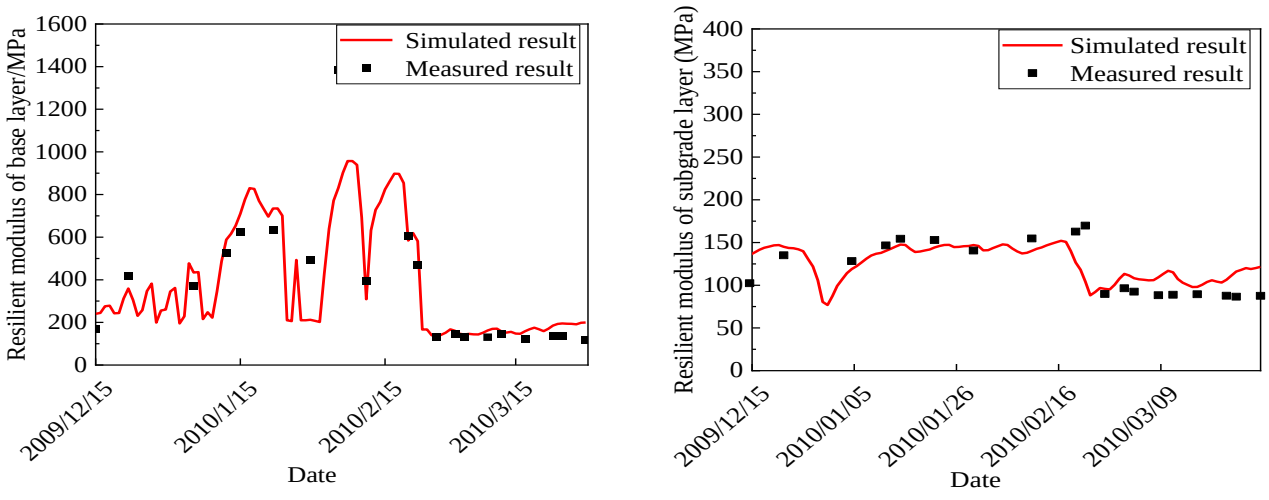


**Figure 14.** Simulated and measured resilient modulus.

To further validate the fatigue life prediction of the Bibi test pavement, the resilient modulus of the pavement will be simulated and verified using two different methods,

including the MEPDG and MEPSCA. The implementation of the MEPDG method is carried out through the AASHTOWare Pavement ME Design [48]. Validating the simulation results of the resilient modulus is crucial because it is a critical parameter in predicting the fatigue life of the pavement. Accuracy (*ACC*) is defined to evaluate the difference between measured and simulated results from the MEPDG or MEPSCA. Equation (37) specifies this term, and a greater accuracy value indicates a better match between the measured and simulated results.

$$ACC = \frac{\sum_{i=1}^{N}\left(1 - \left|\frac{u_i - z_i}{u_i}\right|\right)}{N} \quad (37)$$

where $u_i$ is the measured resilient modulus of $i$-th measurement; $z_i$ is the simulated resilient modulus of $i$-th measurement; and $N$ is the number of measurements.

After examining the comparison results presented in Figures 15 and 16, it appears that both the MEPSCA and MEPDG can predict the resilient modulus of the pavement well. However, the MEPSCA method seems to calculate a daily representative resilient modulus, which can offer more precise and applicable results than a monthly representative value. This is because daily calculations can account for more extreme impacts of freezing–thawing and changes in water content on the resilient modulus, which can significantly influence the performance of pavement structures. In addition, the accuracy of the daily calculations exceeds 0.8, which indicates that the MEPSCA is a reliable method for predicting the resilient modulus.

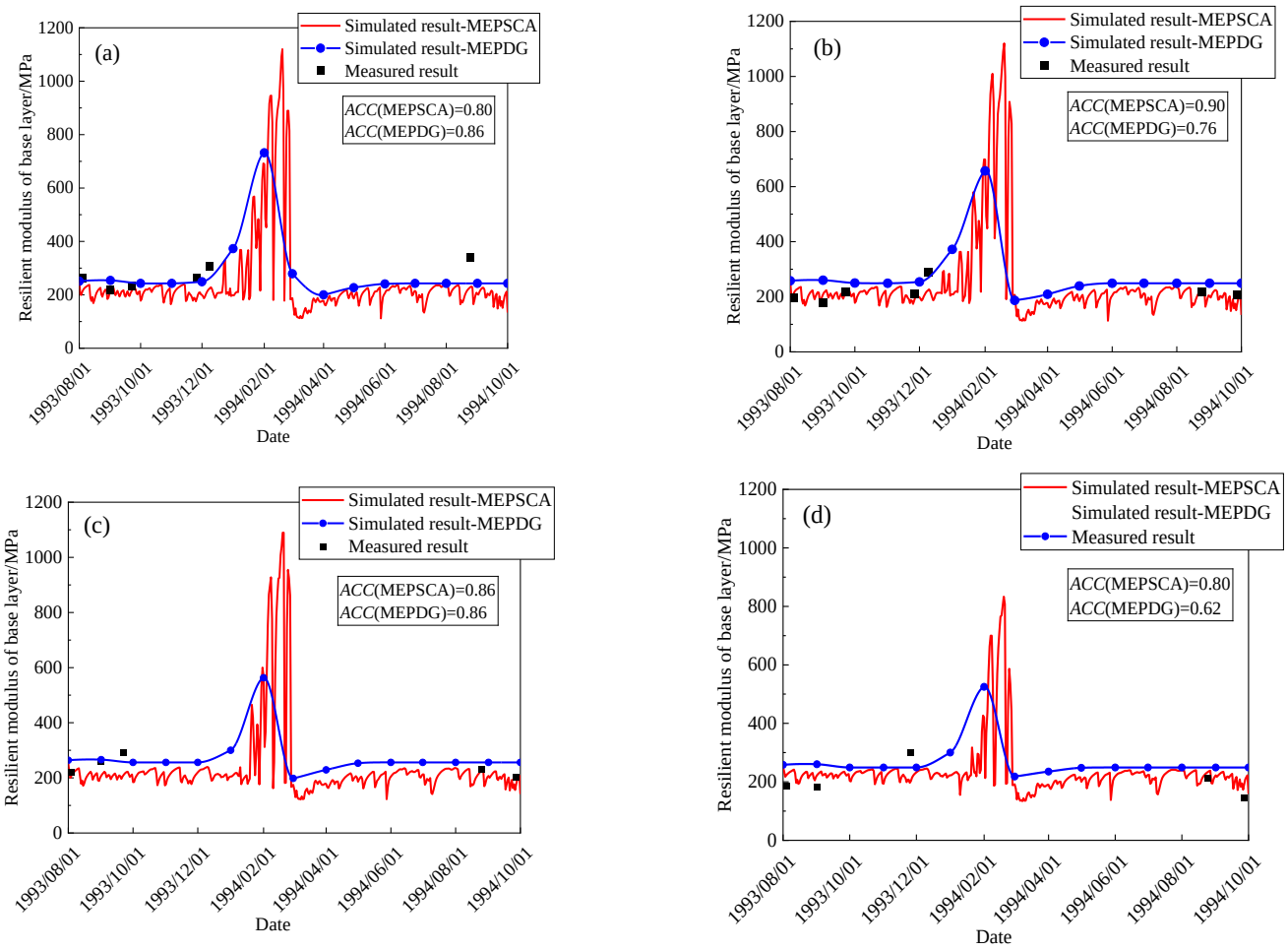


**Figure 15.** Simulated and measured resilient modulus of base course layer ((**a**). section A; (**b**). section B; (**c**). section C; (**d**). section D).

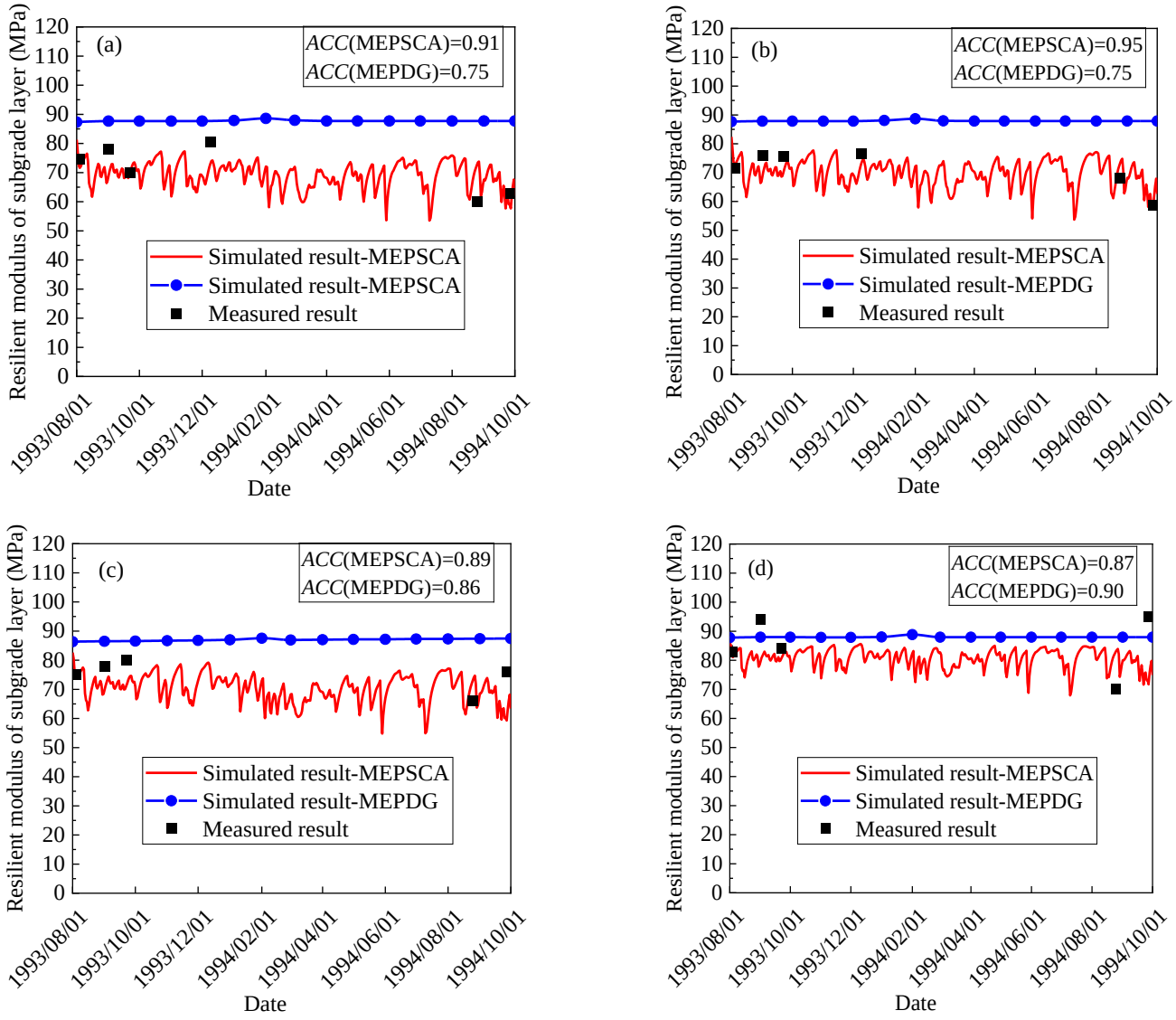


**Figure 16.** Simulated and measured resilient modulus of subgrade layer ((**a**). section A; (**b**). section B; (**c**). section C; (**d**). section D).

## 5. Fatigue Life Evaluation Considering the Environmental Impacts

### *5.1. Predicted Fatigue Life with TPSDM and MEPSCA*

Field examinations and evaluations of most pavements found that fatigue cracking and rutting are the most significant pavement distresses [49,50]. The TPSDM utilizes Equations (38)–(48) to establish criteria for pavement failure caused by rutting and fatigue cracking [4]. These criteria are then used to calculate the allowable numbers of equivalent 49-kN wheel loads for rutting ($N_{fs}$) and fatigue cracking ($N_{fa}$). The design process employs a TPSDM method that utilizes a simplified three-layered model consisting of the As, base course, and subgrade layers, as illustrated in Figure 17.

$$N_{fs} = \beta_{s1} \cdot \left\{ 1.365 \times 10^{-9} \cdot {\varepsilon_a}^{-4.477 \cdot \beta_{s2}} \right\} \tag{38}$$

$$\beta_{s1} = 2134 \tag{39}$$

$$\beta_{s2} = 0.819 \tag{40}$$

$$N_{fa} = \beta_{a1} \cdot C_a \cdot \left\{ 6.167 \times 10^{-5} \cdot \varepsilon_t^{-3.291 \cdot \beta_{a2}} \cdot E_1^{-0.854 \cdot \beta_{a3}} \right\} \quad (41)$$

$$C_a = 10^M \quad (42)$$

$$M = 4.84 \times \left( \frac{VFA}{100} - 0.69 \right) \quad (43)$$

$$\beta_{a1} = K_a \times \beta_{a1} \quad (44)$$

$$K_a = \begin{cases} \frac{1}{8.27 \times 10^{-11} + 7.83 \cdot e^{-0.11 H_a}}, H_a < 18\ cm \\ 1, H_a \geq 18\ cm \end{cases} \quad (45)$$

$$\beta_{a1} = 5.229 \times 10^4 \quad (46)$$

$$\beta_{a2} = 1.314 \quad (47)$$

$$\beta_{a3} = 3.018 \quad (48)$$

where $\beta_{s1}$, $\beta_{s2}$, $\beta_{a1}$, $\beta_{a2}$, and $\beta_{a3}$ are the compensation rates for failure criteria based on the actual situation of Japanese pavement; $C_a$ is the material parameter; $M$ is a factor that relates the $VFA$ to $C_a$; $VFA$ is Voids Filled with Asphalt; $K_a$ is a correction factor, which relates to the thickness of asphalt mixture, $H_a$; $\varepsilon_a$ is the compressive strain on the top surface of the subgrade layer; and $\varepsilon_t$ is the tensile strain on the lower surface of the As layer.

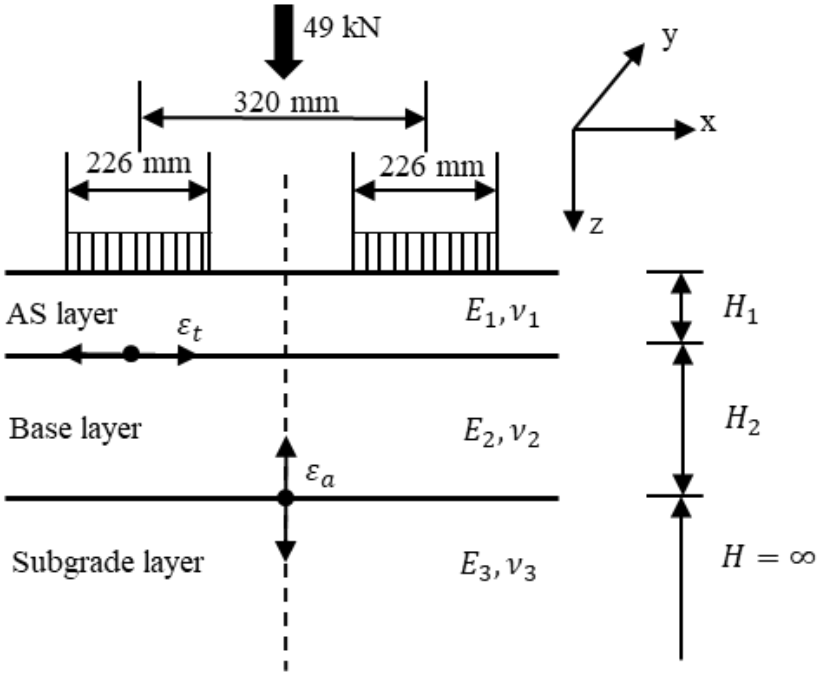


**Figure 17.** Three-layered model for allowable loading number calculation.

In the TPSDM, the monthly representative $E_1$ and constant $E_2$ and $E_3$ are used to calculate the allowable loading number under monthly temperature conditions [4]. However, in contrast, the MEPSCA employs the resilient modulus that varies with environmental impacts and stress states to determine the daily allowable loading number. As a result,

the failure loading number, $N_{fs,i}$ and $N_{fa,i}$ are calculated using Equations (49) and (50), respectively, the primary difference being that $k$ represents either months or days.

$$D_{a,s} = \sum_{i=1}^{k} \frac{N_i}{N_{fa,i}} \tag{49}$$

$$N_{f,d} = \frac{1}{D_{a,s}} \tag{50}$$

where $k$ is the number of environmental conditions, taken as 12 months in the TPSDM and 365 days in the MEPSCA.

### *5.2. MEPDG Rutting Predicting Model*

To overcome the limitations of the Japanese rutting failure criterion explained in the introduction, Lin et al. [16] modified the failure criteria of the TPSDM (Equations (51) and (52)), referring to the MEPDG rutting depth prediction model. Similarly, this study introduced a daily adjustment parameter ($\beta_m$) to modify the MEPCA model, resulting in the development of the MEPSCA-MEPDG model.

$$N_{fs} = \beta_m \cdot \beta_{s1} \cdot \left\{ 1.365 \times 10^{-9} \cdot {\varepsilon_a}^{-4.477 \cdot \beta_{s2}} \right\} \tag{51}$$

$$\beta_m = A_2 + \frac{A_1 - A_2}{1 + (\varepsilon_a / x_0)^p} \tag{52}$$

where $A_1$, $A_2$ are lower and upper limits of $\beta_m$, equal to 0.00493 and 0.67672, respectively; $x_0$ is the fitting parameter, equal to 0.03; and $p$ is fitting parameter, equal to 2.61871.

The MEPSCA-MEPDG model is compared to the TPSDM and MEPSCA models, and the results are presented in Figure 18. As shown in Figure 18, the MEPSCA-MEPDG model can predict significantly smaller $N_{fs}$ than the other two models. It is worth noting that the MEPSCA-MEPDG model has demonstrated its advantages over the other two models in predicting $N_{fs}$. However, there are still some deviations compared to the actual $N_{fs}$, which suggests that other factors that need to be identified may affect the mechanical response. It is important to continue refining and improving the model to minimize the deviations between predicted and actual results.

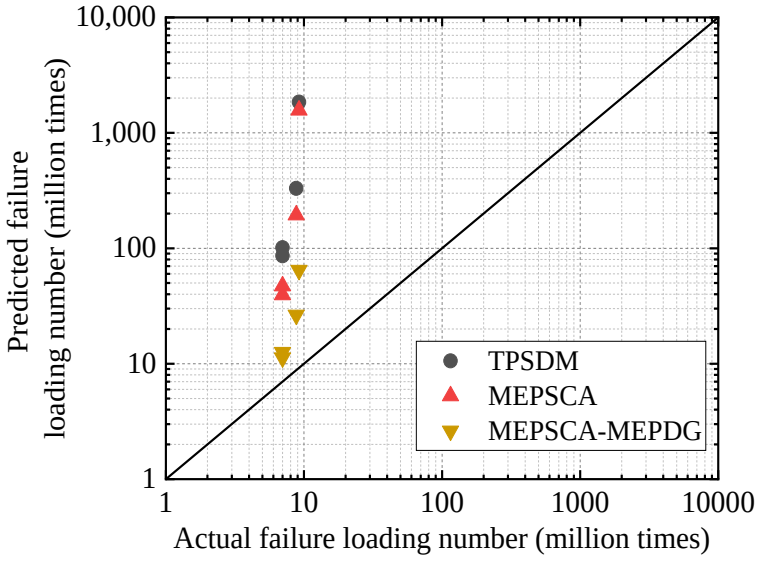


**Figure 18.** Predicted $N_{fs}$ and actual failure loading number.

*5.3. Principal Stress Axis Rotation*

The stress history of each pavement element varies based on its position, as shown in Figure 19. As the wheel loads approach the element under consideration, the principal stresses act obliquely, resulting in positive shear stress. This shear stress intensifies as the load approaches a specific point where the effect of oblique loading decreases and becomes zero when the load is directly above the element. Upon moving away from the element, the shear stress turns negative and increases as the principal stresses become oblique, decreasing as the load moves further away. In addition, the vertical stresses increase until the wheel load is above the element and decrease as it moves away from it.

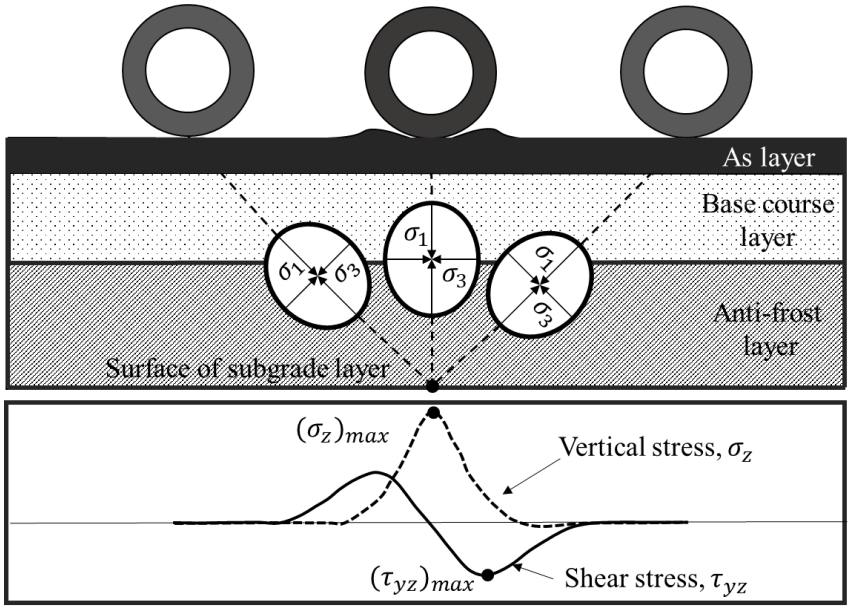


**Figure 19.** Stress variation of pavement under moving wheel loads.

To investigate the permanent strain amplification caused by principal stress axis rotation, Lin et al. conducted tests using a multi-ring shear apparatus and subsequently modified the proposed model using Equations (53) and (54) [16]. Based on the findings, the present study further modified the MEPCA-MEPDG model by incorporating daily axial strain ratios, resulting in the development of the MEPSCA-MEPDG-PASR model.

$$(R_s)_{ave} = exp(\beta_{PASR} \frac{(\tau_{yz})_{max}}{(\sigma_z)_{max}}) \tag{53}$$

$$N_{fs} = \beta_m \cdot \beta_{s1} \cdot \left\{ 1.365 \times 10^{-9} \cdot \varepsilon_a{}^{-4.477 \cdot \beta_{s2}} \right\} / (R_s)_{ave} \tag{54}$$

where $(R_s)_{ave}$ is the ratio of axial strain; $(\sigma_z)_{max}$ is maximum vertical stress at surface of subgrade layer; $(\tau_{yz})_{max}$ is the maximum shear stress at surface of subgrade layer; and $\beta_{PSAR}$ is the material constant.

Figure 20 illustrates the correction effect of the MEPSCA model, highlighting the significant amplification effect of the PASR effect on the mechanical response of pavements. It indicates that the MEPSCA-MEPDG-PASR model can predict values much closer to the actual fatigue life, thus affirming its reliability for predicting fatigue life. The PASR effect has demonstrated its potential to improve the accuracy of the proposed model.

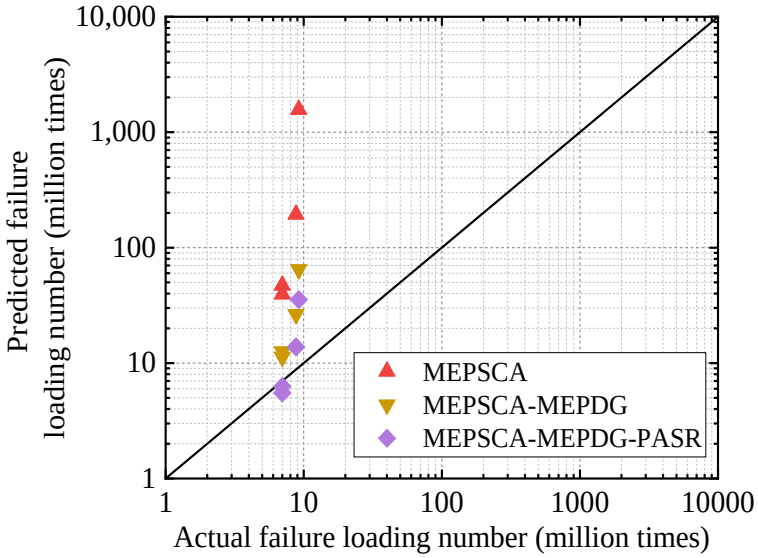


**Figure 20.** Predicted $N_{fs}$ and actual failure loading number.

### *5.4. Variation of Fatigue Life Prediction*

The three fatigue life prediction models mentioned earlier consider environmental impacts, the MEPDG rutting model, and the PASR effect of modifying the current Japanese theoretical pavement structure design method. To enhance the clarity and comprehensiveness of the discussion on fatigue life prediction models for pavement structures, this section will summarize the various models developed previously. Additionally, Figures 21 and 22 illustrate the values of $N_{fs}$ and $N_{fa}$ for the Bibi test pavement under these models, along with the reduction rate of fatigue life ($R_{Nf}$) and the absolute errors of the various prediction models. Figures 21 and 22 provide a visual representation of the performance of the different models in predicting the fatigue life of pavement structures. $R_{Nf}$ is used to represent the ratio of three modified models predicting fatigue life to the TPSDM predicting fatigue life, as defined in Equation (55). All $R_{Nf}$ values are less than 1, indicating that environmental impacts, the MEPDG rutting prediction model, and PASR effects will reduce the fatigue life of the pavement. As fatigue cracking failure was not observed in sections C and D during their service life, there is no actual measured $N_{fa}$ for these two sections in the comparison results. Moreover, according to the results predicted by MEPDG, fatigue cracking failure did not occur in sections C and D. Nonetheless, the $N_{fa}$ obtained from other sections provides valuable insights into the performance of the different fatigue life prediction models.

$$R_{Nf} = \frac{N_{fs}\ (Modified\ model)}{N_{fs}\ (TPSDM)} \tag{55}$$

In the fatigue life against rutting calculation results, $R_{Nf}$ for the MEPSCA, MEPSCA-MEPDG, and MEPSCA-MEPDG-PASR models are around 58.3%, 9.2%, and 4.6%, respectively. The $N_{fs}$ decreased by 41.7% when accounting for the environmental impacts. Furthermore, applying the MEPDG rutting prediction model further reduces the $N_{fs}$ by 49.1%. Finally, considering the PASR effect results in an additional decrease of 4.6% in the $N_{fs}$. In the fatigue life against fatigue cracking calculation results, $R_{Nf}$ caused by the environmental impacts is around 56.8%. In other words, the environmental impact on pavement materials decreases $N_{fa}$ by about 43.2%. These results suggest that these prediction models enhance the applicability and effectiveness of TPSDM by accounting for environmental impacts and traffic load actions on pavement materials.

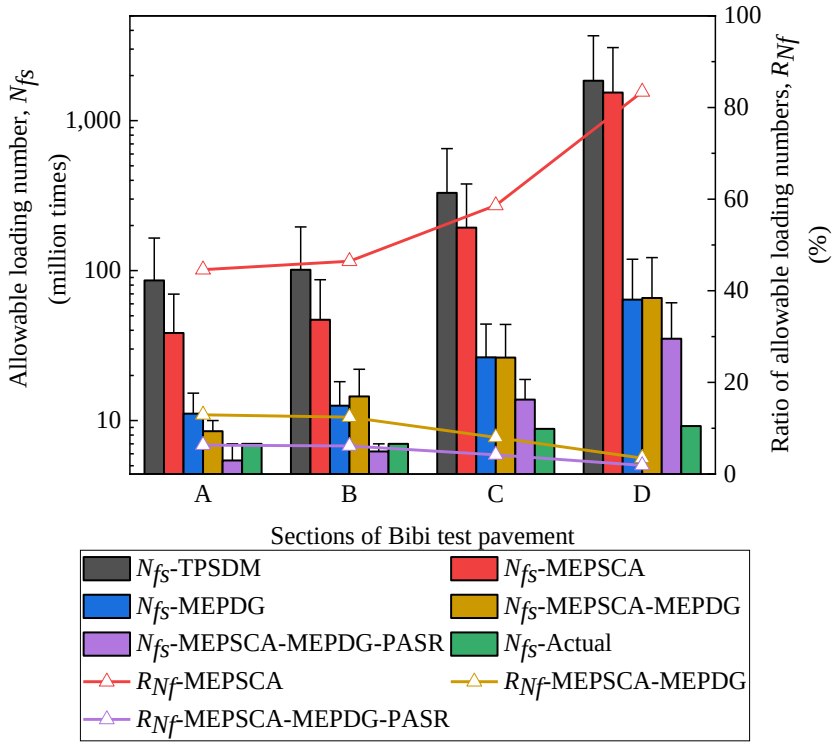


**Figure 21.** Comparison of $N_{fs}$ for different sections under various fatigue life prediction models.

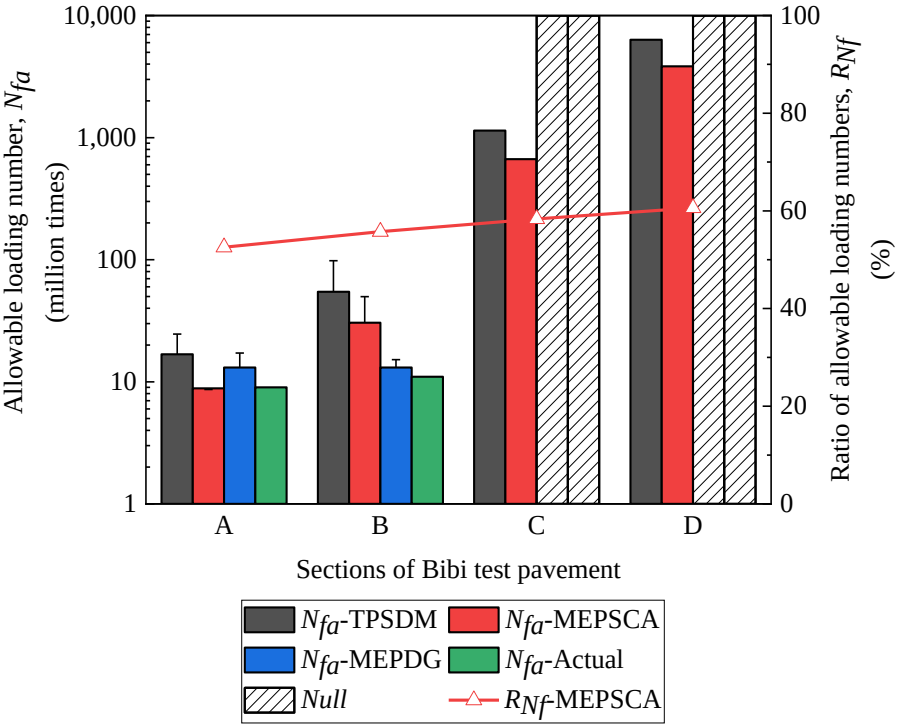


**Figure 22.** Comparison of $N_{fa}$ for different sections under various fatigue life prediction models.

## 6. Conclusions

This study aims to explore the mechanical response and fatigue life prediction of asphalt pavement in cold regions through THM coupling simulation. Through the analysis of experimental data and the comparison of numerical simulation results, the following conclusions can be drawn:

I. The proposed THM simulation method can accurately reproduce the changes in temperature and water content of asphalt pavement, which is the prerequisite for accurately predicting the resilient modulus. The study also analyzed the environmental impacts that cause changes in the thermal and hydraulic fields of pavements and proposed corresponding methods to determine the physical state of each pavement element. These findings demonstrate the potential of THM simulation methods in better understanding physical processes.

II. Based on relevant experimental results, the relationship between resilient modulus, environmental impacts, physical state, and stress state can be established. The application of ODEs and weak-form PDEs can effectively address the challenge of geomaterials physical state changes and the cyclic dependency between resilient modulus, environmental impacts, and stress states. From the distribution of the resilient modulus in the selected typical five seasons, it can be found that the As layer shows a resilient modulus distribution varying with depth, which is mainly due to the ground temperature. For the base course layer, resilient modulus increases as the depth increase due to the bulk stress of soils increasing, and the octahedral shear stress is weakened along with the depth. Under the center of wheel loads, the resilient modulus at the surface of the base course layer changes significantly due to the stress concentration in this area.

III. Combining the time history curve of the resilient modulus, freeze–thaw action, and fluctuation in water content significantly impacts the resilient modulus. On rainy days and during the thawing season, the sudden increase in water content leads to a significant decrease in the resilient modulus inside the pavement. During partial thawing seasons, due to the decrease in permeability in the frozen area, a sandwich structure with reduced resilient modulus will be formed on the surface of the frozen area, which may seriously affect the fatigue life of pavements. On the other hand, the resilient modulus in the pavement increases significantly in the freezing season.

IV. By replacing the constant elastic modulus of the pavement materials in the TPSDM with the resilient modulus related to the stress state and environmental impacts, the fatigue life of pavements against rutting and fatigue cracking is calculated. The results show that water fluctuations and freeze–thaw action will significantly reduce the fatigue life of the pavement in cold regions by reducing the resilient modulus of geomaterials. In addition, introducing the PASR effect and the MEPDG rutting prediction model, the addition of daily axial strain ratio ($(R_s)_{ave}$), and daily adjustment parameter $\beta_m$ to the rutting failure criterion further improve the prediction accuracy and applicability of the modified model.

This study highlights the importance of understanding the mechanical response and fatigue life prediction of asphalt pavement in cold regions through THM coupling simulation. The findings of this study can be used to improve the design of asphalt pavements in cold regions and to prevent issues of over-design and under-design. The proposed method provides a framework for continuous improvement, and it is recommended to conduct further and more comprehensive research to improve the model, including exploring the impact of frost heave and thaw settlement on pavement fatigue life.

**Author Contributions:** Conceptualization, T.I.; Software, J.S.; Formal analysis, J.S.; Investigation, D.R., K.M. and C.U.; Data curation, J.S.; Writing—original draft, J.S.; Writing—review & editing, T.I.; Visualization, J.S.; Supervision, T.I. and K.M.; Project administration, T.I. All authors have read and agreed to the published version of the manuscript.

**Funding:** This research was funded by Japan Society for the Promotion of Science ((B) (19H02234), (A) (20H00266)).

**Institutional Review Board Statement:** Not applicable.

**Informed Consent Statement:** Not applicable.

**Data Availability Statement:** Data sharing not applicable.

**Acknowledgments:** The authors would like to extend their sincere appreciation to the Japan Society for the Promotion of Science (JSPS) KA-KENHI for funding support. The authors would also like to express appreciation to CERI and NEXCO RI (Nippon Expressway Research Institute Company Limited) for their valuable support and contributions to this study.

**Conflicts of Interest:** The authors declare no conflict of interest.

## References

1. Takahashi, S.; Ono, Y.; Sato, M. Field survey to identify the important key factors for long term durability of asphalt pavement on expressways in Japan. *Jpn. Soc. Civ. Eng. Annu. Meet E* **2015**, *71*, 93–101. (In Japanese) [CrossRef]
2. Kabir, T.; Tighe, S. Construction and performance evaluation of polyurethane-bound porous rubber pavement (prp) trial section in the cold climate. *Sustainability* **2023**, *15*, 2413. [CrossRef]
3. AASHTO. *Mechanistic-Empirical Pavement Design Guide: A Manual of Practice*; American Association of State Highway and Transportation Officials: Washington, DC, USA, 2008.
4. Japan Road Association. *Pavement Design Manual*; Japan Road Association: Tokyo, Japan, 2006. (In Japanese)
5. Clayton, C. Stiffness at small strain: Research and practice. *Géotechnique* **2011**, *61*, 5–37. [CrossRef]
6. Seed, H.B.; Chan, C.K.; Monismith, C.L. Effects of repeated loading on the strength and deformation of compacted clay. *Highw. Res. Board Proc.* **1955**, *34*, 541–558.
7. Cole, D.M.; Irwin, L.H.; Johnson, T.C. Effect of freezing and thawing on resilient modulus of a granular soil exhibiting nonlinear behavior. *Transp. Res. Rec.* **1981**, *809*, 809–818.
8. Johnson, T.C.; Cole, D.M.; Chamberlain, E.J. *Influence of Freezing and Thawing on the Resilient Properties of a Silt Soil Beneath an Asphalt Concrete Pavement*; CRREL Report; U.S. Cold Regions Research and Engineering Laboratory: Hanover, NH, USA, 1978; Volume 78, p. 23.
9. Simonsen, E.; Isacsson, U. Soil behavior during freezing and thawing using variable and constant confining pressure triaxial tests. *Can. Geotech. J.* **2001**, *38*, 863–875. [CrossRef]
10. Simonsen, E.; Janoo, V.C.; Isacsson, U. Resilient properties of unbound road materials during seasonal frost conditions. *J. Cold Reg. Eng.* **2002**, *16*, 28–50. [CrossRef]
11. Ishikawa, T.; Lin, T.; Kawabata, S.; Kameyama, S.; Tokoro, T. Effect evaluation of freeze-thaw on resilient modulus of unsaturated granular base course material in pavement. *Transp. Geotech.* **2019**, *21*, 100284. [CrossRef]
12. Peng, J.; Zhang, J.; Li, J.; Yao, Y.; Zhang, A. Modeling humidity and stress-dependent subgrade soils in flexible pavements. *Comput. Geotech.* **2020**, *120*, 103413. [CrossRef]
13. Vaitkus, A.; Gražulytė, J.; Skrodenis, E.; Kravcovas, I. Design of frost resistant pavement structure based on road weather stations (rwss) data. *Sustainability* **2016**, *8*, 1328. [CrossRef]
14. NCHRP. *Guide for Mechanistic-Empirical Design of New and Rehabilitated Pavement Structures*; National Cooperative Highway Research Program: Washington, DC, USA, 2004.
15. Lin, T.; Ishikawa, T.; Yang, J.; Tokoro, T. Evaluation of climate effect on resilient modulus of granular subgrade material. *Cold Reg. Sci. Technol.* **2022**, *194*, 103452. [CrossRef]
16. Lin, T.; Ishikawa, T.; Maruyama, K.; Tokoro, T. Pavement design method in Japan with consideration of climate effect and principal stress axis rotation. *Transp. Geotech.* **2021**, *28*, 100552. [CrossRef]
17. Gräbe, P.; Clayton, C. Effects of principal stress rotation on permanent deformation in rail track foundations. *J. Geotech. Geoenvironmental Eng.* **2009**, *135*, 555–565. [CrossRef]
18. Shabani, F.; Kaviani-Hamedani, F. Cyclic response of sandy subsoil layer under traffic-induced principal stress rotations: Application of bidirectional simple shear apparatus. *Soil Dyn. Earthq. Eng.* **2023**, *164*, 107573. [CrossRef]
19. Lekarp, F.; Dawson, A. Modelling permanent deformation behaviour of unbound granular materials. *Constr. Build. Mater.* **1998**, *12*, 9–18. [CrossRef]
20. Miura, K.; Miura, S.; Toki, S. Deformation behavior of anisotropic dense sand under principal stress axes rotation. *Soils Found.* **1986**, *26*, 36–52. [CrossRef]
21. *COMSOL Multiphysics®*, Version 6.1; COMSOL Multiphysics: Stockholm, Sweden, 2021. Available online: www.comsol.com(accessed on 1 March 2021).
22. Sheppard, M.; Kay, B.; Loch, J. Development and testing of a computer model for heat and mass flow in freezing soils. In Proceedings of the International Conference on Permafrost, Edmonton, AB, Canada, 10–13 July 1978; pp. 75–81.
23. De Vries, D.A. Simultaneous transfer of heat and moisture in porous media. *Trans. Am. Geophys. Union* **1958**, *39*, 909–916. [CrossRef]
24. David, M.P.; Lidija, Z. *Finite Element Analysis in Geotechnical Engineering: Theory*, 1st ed.; Thomas Telford: London, UK, 1999.
25. Van Genuchten, M.T. A closed-form equation for predicting the hydraulic conductivity of unsaturated soils. *Soil Sci. Soc. Am. J.* **1980**, *44*, 892–898. [CrossRef]
26. Côté, J.; Konrad, J.M. A generalized thermal conductivity model for soils and construction materials. *Can. Geotech. J.* **2005**, *42*, 443–458. [CrossRef]

27. Johnston, G.H.; Ladanyi, B.; Morgenstern, N.R.; Penner, E. Engineering characteristics of frozen and thawing soils. In *Permafrost Engineering Design and Construction*, 1st ed.; Johnston, G.H., Ed.; John Wiley Sons: Toronto, ON, Canada, 1981.
28. Dall'Amico, M.; Endrizzi, S.; Gruber, S.; Rigon, R. A robust and energy-conserving model of freezing variably-saturated soil. *Cryosphere* **2011**, *5*, 469–484. [CrossRef]
29. Zhang, Y.; Gu, F.; Luo, X.; Birgisson, B.; Lytton, R.L. Modeling stress-dependent anisotropic elastoplastic unbound granular base in flexible pavements. *Transp. Res. Rec.* **2018**, *2672*, 46–56. [CrossRef]
30. Shimata, A.; Nakagawa, S.; Takahashi, M. The study of long term performance of pavements at the bibi test road. *J. Pavement Eng.* **1996**, *1*, 197–204. (In Japanese) [CrossRef]
31. Kojima, K. Snowmelt mechanism and heat balance. *Kishou Kenkyuu Note* **1979**, *136*, 1–38. (In Japanese)
32. Zhu, Y. Wide-area geohazard risk assessment in snowy-cold regions by multiphase soil mechanics and multi-scale analysis. Doctoral Dissertation, Hokkaido University, Sapporo, Japan, 2020.
33. Shinme, R.; Yamashita, S. Hydrologic measurement using snowcover weightmeter in winter. *Proc. Hydraul. Eng.* **2008**, *52*, 493–498. [CrossRef]
34. Endo, A. A question of snow density and maximum snow depth. *J. Jpn. Assoc. Snow Eng.* **1986**, *2*, 23–30. (In Japanese)
35. Japan Meteorological Agency. Automated Meteorological Data Acquisition System. 2020. Available online: https://www.jma.go.jp/jp/amedas/ (accessed on 5 December 2020).
36. Andersland, O.B.; Ladanyi, B. *Frozen Ground Engineering*, 2nd ed.; John Wiley & Sons: Hoboken, NJ, USA, 2003.
37. Doré, G.; Zubeck, H.K. *Cold Regions Pavement Engineering*, 1st ed.; ASCE Press: Reston, VA, USA, 2009.
38. Zarling, J.P.; Braley, W.A. Embankment design and construction in cold regions. In *Geotechnical Thermal Analysis*; Johnson, E.G., Phukan, A., Haas, W.H., Eds.; ASCE Press: Reston, VA, USA, 1988.
39. Bras, R.L. *Hydrology: An Introduction to Hydrologic Science*; Addison Wesley Publishing Company: Boston, MA, USA, 1990.
40. Takeichi, K.; Kubo, H.; Kasahara, A. A Pavement design for low-volume roads that considers the antifrost effects of thickly packed snow. *Transp. Res. Rec.* **1987**, *1*, 237.
41. Furuki, T.; Ishikawa, T.; Kobe, H.; Ochi, Y. Proposal of capillary barrier system by size optimization of asphalt pavement. *Annu. Meet. JGS Hokkaido Branch* **2022**, *62*, 67–76. (In Japanese)
42. Kaneko, H.; Ishikawa, T.; Nakamura, T.; Kishitani, I.; Hiramatsu, K. Effect of ageing on rainfall infiltration characteristics of unsaturated granular roadbeds. *Annu. Meet. JGS Hokkaido Branch* **2021**, *61*, 165–172. (In Japanese)
43. Pavement Engineering Committee. *Problems and Countermeasures of Pavement in Snowy Cold Regions*, 1st ed.; JSCE Press: Tokyo, Japan, 2016. (In Japanese)
44. Zhang, H.; Ma, S.; Yu, T. Comparative study on HMA elastic modulus based on different predicting methods. *J. Chongqing Jiaotong Univ. (Nat. Sci.)* **2018**, *37*, 35–39. (In Chinese)
45. Fan, Y.; Wu, Y.; Chen, H.; Liu, S.; Huang, W.; Wang, H.; Yang, J. Performance evaluation and structure optimization of low-emission mixed epoxy asphalt pavement. *Materials* **2022**, *15*, 6472. [CrossRef]
46. Pavement Engineering Committee. *FWD and Small FWD Operational Guide*, 3rd ed.; JSCE Press: Tokyo, Japan, 2002. (In Japanese)
47. Kim, D.S.; Kweon, G.C.; Lee, K.H. Alternative method of determining resilient modulus of compacted subgrade soils using free-free resonant column test. *Transp. Res. Rec.* **1997**, *1577*, 62–69. [CrossRef]
48. *AASHTOWare®*, Version 2.6; AASHTOWare Pavement ME Design: Champaign, IL, USA, 2021. Available online: https://me-design.com/MEDesign/(accessed on 1 May 2022).
49. Abdullah, G.M. Performance of enhanced problematic soils in roads pavement structure: Numerical simulation and laboratory study. *Sustainability* **2023**, *15*, 2595. [CrossRef]
50. Perić, D.; Goh, G.; Saeidaskari, J.; Rashk Olia, A.S.; Ayar, P. Development of prediction models for performance of flexible pavements in kansas with emphasis on the effects of subgrade and unbound layers. *Sustainability* **2022**, *14*, 9020. [CrossRef]